PHYSICS OF FLUIDS **28**, 095101 (2016)

Dynamic unified RANS-LES simulations of high Reynolds number separated flows

Reza Mokhtarpoor,[1] Stefan Heinz,[1,a)] and Michael Stoellinger[2]
[1]*Department of Mathematics, University of Wyoming, 1000 E. University Avenue, Laramie, Wyoming 82071, USA*
[2]*Department of Mechanical Engineering, University of Wyoming, 1000 E. University Avenue, Laramie, Wyoming 82071, USA*

(Received 12 May 2016; accepted 3 August 2016; published online 1 September 2016)

The development of hybrid RANS-LES methods is seen to be a very promising approach to enable efficient simulations of high Reynolds number turbulent flows involving flow separation. To contribute to further advances, we present a new, theoretically well based, dynamic hybrid RANS-LES method, referred to as DLUM. It is applied to a high Reynolds number flow involving both attached and separated flow regimes: a periodic hill flow is simulated at a Reynolds number of 37 000. Its performance is compared to pure LES, pure RANS, other hybrid RANS-LES (given by DLUM modifications), and experimental observations. It is shown that the use of this computational method offers huge cost reductions (which scale with $Re/200$, Re refers to the Reynolds number) of very high Reynolds number flow simulations compared to LES, it is much more accurate than RANS, and more accurate than LES, which is not fully resolved. In particular, this conclusion does also apply to the comparison of DLUM and pure LES simulations on rather coarse grids, which are often simply required to deal with simulations of very high Reynolds number flows: the DLUM provides mean velocity fields which are hardly affected by the grid, whereas LES velocity fields reveal significant shortcomings. We identified the reason for the superior performance of our new dynamic hybrid RANS-LES method compared to LES: it is the model's ability to respond to a changing resolution with adequate turbulent viscosity changes by ensuring simultaneously a physically correct turbulence length scale specification under the presence of interacting RANS and LES modes. *Published by AIP Publishing.* [http://dx.doi.org/10.1063/1.4961254]

I. INTRODUCTION

One of the biggest challenges of computational fluid dynamics is the accurate and feasible simulation of very high Reynolds number flows involving flow separation. Such simulations are needed, for example, to improve the optimization of aircraft flight and wind turbine performance. The application of direct numerical simulation (DNS) for such flow computations is infeasible for the foreseeable future, and large-eddy simulation (LES) also is computationally too expensive with respect to the majority of such applications.[1] The alternative use of Reynolds-averaged Navier-Stokes (RANS) equations suffers from major shortcomings if such equations are applied to separated flows because of the inability of RANS equations to correctly simulate instantaneous coherent structures (recirculation regions) in turbulent flows.

One approach to address these problems is given by the development of wall-modeled LES (WMLES).[2–8] This approach focuses on providing a synthetic boundary condition at some distance off the wall instead of the no-slip velocity condition at the wall. This enables the use of relatively coarse grids, which significantly reduces the computational cost. Recently developed

a)Author to whom correspondence should be addressed. Electronic mail: heinz@uwyo.edu

techniques enable accurate simulations of flat-plate turbulent boundary layers (including separation and reattachment) up to relatively high Reynolds numbers.[3,7] With respect to simulations of periodic hill flow including separation at a relatively low Reynolds number (Re = 10 595) corresponding to the higher Reynolds number case considered here, a comparison of three WMLES[2,4,5] was presented by Balakumar *et al.*[6] These studies demonstrate promising capabilities of WMLES regarding such flow simulations, but they also indicate the need for further methodological improvements to accomplish accurate WMLES simulations of complex turbulent flows including separation.

Another approach to overcome the problems described in the first paragraph is the combination of RANS and LES methods to take advantage of both the computational efficiency of RANS equations and the ability of LES to resolve large scale flow structures and to simulate coherent instantaneous structures. There is a huge variety of suggestions of how hybrid RANS-LES methods should be designed, see, for example, Refs. 1 and 9–45. Some methods have a sound theoretical basis, whereas other methods are based on purely empirical arguments. Given the many alternative formulations and ongoing research over two decades, we have to expect that the analysis, improvement, and comparison of different approaches will continue for a relatively long time. In particular, there is growing evidence that the main problem of this research is the understanding of basic mechanisms of a computational method that is neither RANS nor LES: the interplay of RANS and LES modes in hybrid RANS-LES methods. The latter interaction is often considered to be the reason for a suboptimal performance of hybrid RANS-LES methods, which may suffer, for example, from a lack of fluctuations in LES regions, or a significant amount of fluctuations that disturb RANS solutions in RANS regions.

The purpose of this paper is to further explore the benefits of hybrid RANS-LES methods based on stochastic analysis.[46,43,44,47,48,45,49,50] Conceptually, this approach has several advantages. First, such equations are based on a stochastic turbulence model that honors the realizability constraint,[51–53] this means the constraint that an acceptable turbulence closure model should be based on the statistics of a velocity field that is physically achievable or realizable. The realizability principle is proven to significantly contribute to the development of accurate turbulence models.[54–62] Second, the underlying stochastic turbulence model implies a hierarchy of simpler models, which can be systematically derived. Third, with respect to hybrid RANS-LES, this modeling approach focuses the hybridization problem to the problem of how scale information is provided to the model, whereas the velocity field is described by the same equations applied in RANS and LES. Fourth, with respect to dynamic LES, this modeling approach enables a formulation of the dynamic coefficient calculation that is consistent with the derivation of LES equations.

So far, the approach described in the preceding paragraph was used separately for performing nondynamic hybrid RANS-LES simulations of turbulent channel flows[45] and swirling turbulent jet flows,[49] and nonhybrid dynamic LES of turbulent channel flows[48] and the turbulent Ekman layer.[50] The purpose of this paper is to present a new computational method: a hybrid RANS-LES model that involves LES dynamically. This computational method is applied to high Reynolds number separated flows which were already used for several studies of the performance of computational methods with respect to separated flow simulations. The following specific questions are considered:

1. With respect to grids that enable resolving simulations, what is performance-wise the difference between the new hybrid RANS-LES model considered and dynamic LES?
2. With respect to much coarser grids, what is performance-wise the difference between the new hybrid RANS-LES model considered and dynamic LES?
3. What is the reason for performance differences between dynamic LES and the new hybrid RANS-LES model?
4. With respect to both the new hybrid RANS-LES model considered and dynamic LES, how does the computational cost of these methods scale with the Reynolds number?

It is worth noting that LES of the high Reynolds number (Re = 37 000) periodic hill flow considered was not reported so far.

The paper is organized in the following way. The equations of the dynamic unified RANS-LES model are introduced in Sec. II, and the flows considered are described in Sec. III. The numerical methods applied, LES, and the dynamic unified RANS-LES model are described in Secs. IV and V. The performance and cost differences of the dynamic unified RANS-LES model and dynamic LES are described in Secs. VI and VII, respectively. The conclusions are summarized in Sec. VIII.

II. DYNAMIC UNIFIED RANS-LES AND DYNAMIC LES EQUATIONS

The theoretical basis of the modeling approach applied is explained in Sec. II A. In Subsections II B and II C, we present the equations for the non-dynamic hybrid RANS-LES model considered, which can be used to perform RANS, LES, and hybrid RANS-LES,[44,45] and its dynamic LES version, which is presented here for the first time. Subsection II D explains how these equations are used in discretized form.

A. Modeling approach

The unified RANS-LES model is based on a realizable stochastic model for turbulent velocities.[46,43,44,47,45] The model implies the exact but unclosed filtered Navier-Stokes equations. This means the conservation of mass and momentum equations implied by the stochastic velocity model are given by

$$\frac{\partial \bar{U}_i}{\partial x_i} = 0, \tag{1}$$

$$\frac{\bar{D}\bar{U}_i}{\bar{D}t} = -\frac{1}{\rho}\frac{\partial \bar{p}}{\partial x_i} + 2\nu\frac{\partial \bar{S}_{ij}}{\partial x_j} - \frac{\partial \tau_{ij}}{\partial x_j}. \tag{2}$$

Here, the overbar refers to ensemble-averaged (RANS) or space-averaged (LES) variables. $\bar{D}/\bar{D}t = \partial/\partial t + \bar{U}_j\partial/\partial x_j$ denotes the filtered Lagrangian time derivative, U_i denotes components of the velocity vector, p is the pressure, ρ is the constant fluid density, ν is the constant kinematic viscosity, and $S_{ij} = (\partial U_i/\partial x_j + \partial U_j/\partial x_i)/2$ is the rate-of-strain tensor. The subgrid-scale (SGS) stress tensor τ_{ij} appears as an unknown on the right hand side of the momentum equation. The sum convention is used throughout this paper. The equations are presented here for incompressible flow. The extension to compressible flow, which is straightforward, can be found elsewhere.[46,43,44,47]

In addition to the continuity Eq. (1) and conservation of momentum Eq. (2), the underlying stochastic velocity model[46,43,44,47] implies for the SGS stress τ_{ij} the equation

$$\frac{\bar{D}\tau_{ij}}{\bar{D}t} + \frac{\partial T_{kij}}{\partial x_k} = -\tau_{ik}\frac{\partial \bar{U}_j}{\partial x_k} - \tau_{jk}\frac{\partial \bar{U}_i}{\partial x_k} - \frac{1}{(1-c_0)\tau}\left(\tau_{ij} - \frac{2}{3}c_0 k\delta_{ij}\right). \tag{3}$$

Here, T_{ijk} is the triple correlation tensor of velocity fluctuations, δ_{ij} refers to the Kronecker symbol, τ is the dissipation time scale of turbulence, and c_0 is a model constant that is specified below (see Eq. (13) and the related discussion in Sec. II C). For the following it is helpful to rewrite Eq. (3) in terms of equations for $k = \tau_{nn}/2$ and standardized anisotropy tensor $d_{ij} = (\tau_{ij} - 2k\delta_{ij}/3)/(2k)$. Here, k refers to the modeled turbulent kinetic energy, this means the turbulent kinetic energy or SGS kinetic energy in RANS and LES, respectively. The k and d_{ij} equations are then given by[44]

$$\frac{\bar{D}k}{\bar{D}t} + \frac{1}{2}\frac{\partial T_{knn}}{\partial x_k} + 2kd_{kn}\frac{\partial \bar{U}_n}{\partial x_k} = -\frac{k}{\tau}, \tag{4}$$

$$\frac{\bar{D}d_{ij}}{\bar{D}t} + \frac{1}{2k}\frac{\partial(T_{kij} - T_{knn}\delta_{ij}/3)}{\partial x_k} + \frac{d_{ij}}{k}\frac{\bar{D}k}{\bar{D}t} + d_{ik}\frac{\partial \bar{U}_j}{\partial x_k} - \frac{2}{3}d_{kn}\frac{\partial \bar{U}_n}{\partial x_k}\delta_{ij} = -\frac{d_{ij}}{(1-c_0)\tau} - \frac{2}{3}\bar{S}_{ij}. \tag{5}$$

The latter equation can be used to derive a hierarchy of algebraic stress models.[44] The simplest model of this hierarchy is given by a linear stress model, which is obtained by assuming a balance of the right-hand side terms of Eq. (5),

$$d_{ij} = -2(1-c_0)\bar{S}_{ij}\tau/3. \tag{6}$$

This expression implies for the SGS stress τ_{ij} the model

$$\tau_{ij} = \frac{2}{3}k\delta_{ij} - 2\nu_t \bar{S}_{ij}, \tag{7}$$

where the turbulent viscosity is given by $\nu_t = 2(1 - c_0)k\tau/3$. By using the stress model Eq. (7), the velocity Eq. (2) reads now

$$\frac{\bar{D}U_i}{\bar{D}t} = -\frac{1}{\rho}\frac{\partial P}{\partial x_i} + 2\frac{\partial(\nu + \nu_t)\bar{S}_{ij}}{\partial x_j}, \tag{8}$$

where $P = (\bar{p} + 2k\rho/3)$ is the modified pressure, and the turbulent kinetic energy Eq. (4) reads now

$$\frac{\bar{D}k}{\bar{D}t} = -\frac{1}{2}\frac{\partial T_{knn}}{\partial x_k} + 2\nu_t \bar{S}_{nk}\bar{S}_{nk} - \frac{k}{\tau}, \tag{9}$$

where the definition of $\bar{S}_{nk}$ is used. To close this equation we use $T_{knn} = -2(\nu + \nu_t)\partial k/\partial x_k$ for triple correlations. The structure of this expression can be derived as a consequence of the transport equation for triple correlations, which is implied by the stochastic velocity model applied.[46,43,44,47] By using this expression for T_{knn}, the turbulent kinetic energy equation can be written as

$$\frac{\bar{D}k}{\bar{D}t} = \frac{\partial}{\partial x_j}\left[(\nu + \nu_t)\frac{\partial k}{\partial x_j}\right] + \nu_t S^2 - \frac{k}{\tau}, \tag{10}$$

where $S = (2\bar{S}_{ij}\bar{S}_{ji})^{1/2}$ refers to the magnitude of the rate-of-strain tensor.

B. The non-dynamic unified RANS-LES model

Equations (8) and (10) are unclosed as long as the time scale τ is not defined. Usually applied RANS and LES equations can be recovered by using $\tau = \tau^{RANS}$ with $\tau^{RANS} = 1/\omega$ for the RANS case, and $\tau = \tau^{LES}$ with $\tau^{LES} = \Delta k^{-1/2}$ for the LES case, respectively. Here, Δ refers to the filter width, which is defined to be the large side filter, $\Delta = \Delta_{max} = \max(\Delta_x, \Delta_y, \Delta_z)$ (a different Δ definition is evaluated in Sec. V C), and ω is the characteristic turbulence frequency. To provide ω we apply for the turbulent frequency the transport equation[63]

$$\frac{\bar{D}\omega}{\bar{D}t} = C_{\omega_1}\frac{\omega}{k}\nu_t S^2 - \frac{C_{\omega_2}}{C_k}\omega^2 + \frac{\partial}{\partial x_j}\left[(\nu + \frac{\nu_t}{\sigma_\omega})\frac{\partial \omega}{\partial x_j}\right] + \frac{C_\omega}{k}(\nu + \nu_t)\frac{\partial k}{\partial x_j}\frac{\partial \omega}{\partial x_j}. \tag{11}$$

Here $C_{\omega 1}$, $C_{\omega 2}$, C_ω, C_k, and σ_ω are model constants that have the values

$$C_{\omega 1} = 0.49,\ C_{\omega 2} = 0.072,\ C_\omega = 1.1,\ C_k = 0.09,\ \sigma_\omega = 1.8.$$

The suitability of these settings was evaluated by comparisons with DNS and other turbulence models with respect to channel flow, a backward-facing step flow and a ribroughened channel flow with heat transfer.[63] The value of ω at the first cells above the wall was set explicitly by using the expression $\omega = 2\nu/d^2$,[63] where d refers to the distance from the wall to the cell center of the first cell.

The unification of RANS and LES models is accomplished by introducing the unified time scale by the relation

$$\tau = min(\tau^{RANS}, \tau^{LES}), \tag{12}$$

where $\tau^{RANS} = 1/\omega$ and $\tau^{LES} = \Delta k^{-1/2}$. This choice is the simplest choice that can be considered. A thorough analysis of other options showed that there is so far no evidence for the benefits of more complex unified time scale definitions.[45] It is worth noting that the RANS-LES transition defined in this way corresponds to a local switch of RANS and LES equations, which fluctuates in space and time (see below). On average, RANS and LES regions are not separated in space but there is an extended zone of interaction of RANS and LES regimes.

C. The dynamic linear unified model (DLUM)

The closure of Eqs. (8), (10), and (11) combined with the incompressibility constraint $\partial \bar{U}_i/\partial x_i = 0$ still requires the definition of $2(1-c_0)/3$ in the SGS viscosity $\nu_t = 2(1-c_0)k\tau/3$. To clearly distinguish between parameter settings in RANS and LES regimes we introduce new parameters for $2(1-c_0)/3$ in RANS and LES modes,

$$\nu_t = \begin{cases} C_\mu k\tau^{RANS} & \text{RANS region} \\ C_d k\tau^{LES} & \text{LES region} \end{cases}. \tag{13}$$

We can compute C_d dynamically if the equations are in LES mode. There is a variety of dynamic LES methods. The advantage of the approach used here is that the dynamic LES method can be designed fully consistent with the LES model applied.[47,48] The basic approach is the following.[47] The stochastic model considered[46,43,44,47] to derive the LES model is upscaled such that this upscaled stochastic model implies test-filtered LES equations. In correspondence to Eq. (7) for the SGS stress, the upscaled stochastic model determines an algebraic model for the deviatoric Leonard stress, which enables the dynamic coefficient calculation based on minimizing the least-squares error. This implies for C_d the relation

$$C_d = -\frac{L^d_{ij}M_{ji}}{M_{kl}M_{lk}}. \tag{14}$$

Here, L^d_{ij} refers to the deviatoric component of the Leonard stress $L_{ij} = \widehat{\bar{U}_i\bar{U}_j} - \hat{\bar{U}}_i\hat{\bar{U}}_j$ (the hat refers to the test filtering), and M_{ij} is given by $M_{ij} = 2\Delta^T\sqrt{k^T}\hat{\bar{S}}_{ij}$, which involves the test-filter turbulent kinetic energy $k^T = L_{nn}/2$ and filter width on the test-filter level $\Delta^T = 2\Delta$. It is worth noting that this dynamic LES model is different from the dynamic Smagorinsky model (DSM). In contrast to M_{ij} applied here, the DSM extends M_{ij} by an additional term. This additional term involves an incorrect dependence on Δ and it contributes to the development of computational instabilities.[47,48] Recent applications to turbulent channel flow simulations[48] and turbulent Ekman layer simulations[50] show significant advantages compared to the use of the stabilized DSM. For the flows considered here it turned out that the values of C_d needed to be bounded from below such that the minimum of C_d cannot be less than -0.5. Figure 1 shows the time history of C_d (obtained by using dynamic LES on the 500K grid) for the last 20 flow-through times at two probe points inside the recirculation region. We see that the lower bound of C_d applied represents an extremely weak limitation. The means and standard deviations of C_d, which are also shown, indicate a significant amount of C_d variations. This can be explained by the fact that C_d is shown in the recirculation region, which is characterized by a significant unsteadiness due to the coherent motions involved.

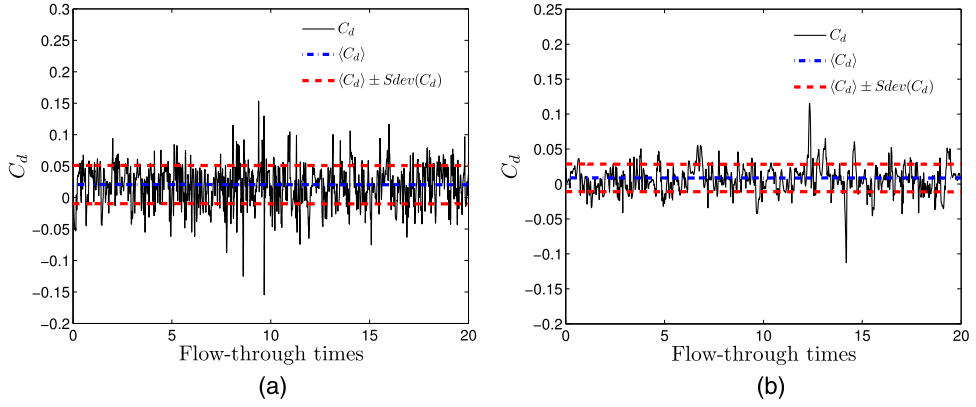

FIG. 1. Time histories of C_d in dynamic LES simulations of the periodic hill flow for the last 20 flow-through times at two different probe points in the recirculation region. The probe point coordinates are (a) $(x, y, z)/h = (2.5, 0.1, 2.25)$ and (b) $(x, y, z)/h = (3.5, 1.0, 2.25)$. The mean values $\langle C_d \rangle = (0.008, 0.020)$ and standard deviations $Sdev(C_d) = (0.02, 0.03)$ of C_d are also shown in (a) and (b), respectively.

In RANS mode, the use of a constant value for C_μ does not account for the damping effect of walls. The inclusion of wall damping effects in C_μ is considered separately in Sec. V A in conjunction with the discussion of the hybrid RANS-LES model. Computationally, C_d and C_μ are applied whenever the model switches to LES or RANS modes, see Sec. II B.

D. Discretization of equations

The dynamic unified RANS-LES model has been implemented in the OpenFOAM CFD Toolbox.[64] The calculations have been performed using a finite-volume based method with the numerical grid being used as the LES filter. The convection term was discretized using a second-order central difference scheme in the momentum equation and a bounded second-order central difference scheme in the turbulence transport equations to ensure a stable solution. All other terms were discretized using a second-order central difference scheme. The pressure gradient that drives the flow in the channel has been adjusted dynamically to maintain a constant mass flow rate. PISO algorithm was used for the pressure-velocity coupling.[65] The resulting algebraic equations for all the flow variables except the pressure have been solved iteratively using a preconditioned bi-conjugate gradient method with a diagonally incomplete LU preconditioning at each time step. The Poisson equation for pressure was solved using an algebraic multi-grid solver. Time marching was performed using a second-order backward difference scheme.

III. THE FLOW CONSIDERED

The flow considered to evaluate the performance of our new DLUM is described next. First, the flow geometry is introduced. Then, previous studies at moderate and high Reynolds numbers, respectively, are described.

A. Periodic hill flows

We consider separated flow over two-dimensional hills as illustrated in Figure 2. This flow configuration creates a variety of relevant flow features such as separation, recirculation, and natural reattachment.

The flow considered follows the numerical work of Mellen *et al.*[66] who adjusted the experimental geometry of Almeida *et al.*[67] to meet numerical needs. Without changing the shape of the hill, the channel height was reduced by a factor of two to decrease the computational cost, and the distance between succeeding hills was doubled to allow for natural reattachment. Moreover, periodicity was assumed in streamwise direction and statistical homogeneity was assumed in spanwise directions to facilitate numerical studies with lower computational cost and to apply simple periodic boundary conditions in streamwise and spanwise directions. After Mellen *et al.*,[66] this geometry has been used for various numerical studies and served as a benchmark for testing the performance of various turbulence models. For example, Temmerman and Leschziner,[68,69] Jakirlic *et al.*,[70] Jang *et al.*,[71] and Fröhlich *et al.*[72] used this flow configuration to test various turbulence models and numerical methods.

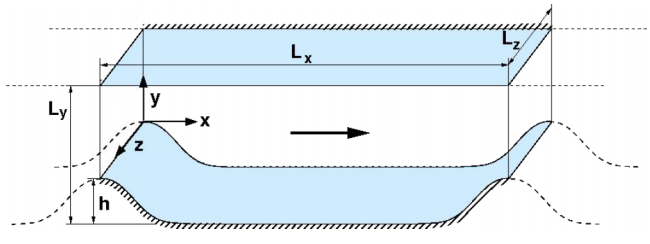

FIG. 2. The geometry of two-dimensional periodic hill flows.[80]

B. Previous studies: Moderate Reynolds numbers

A comprehensive numerical study of the periodic hill flow at $Re = 10\,595$ was carried out by Fröhlich *et al.*[72] using two different LES codes and a grid with 4.6×10^6 points. At this time, the flow was only investigated numerically because reliable experimental data were unavailable. To overcome this deficiency, a water channel was set up in the Hydromechanik Laboratorium of the Technische Universität München. First experimental results were presented by Rapp and Manhart[73] and Rapp *et al.*[74]

Extensive numerical and experimental studies for a range of Reynolds number $100 \leq Re \leq 10\,595$ were performed then by Breuer *et al.*[75] In particular, DNS of this flow was carried out by this group at $Re = 700, 1400, 2800, 5600$ on several grids,[75] and LES of this flow was performed at $Re = 10\,595$ using 13.1×10^6 grid points.

Jakirlic *et al.*[76] carried out zonal and seamless hybrid RANS-LES simulations based on the $k - \varepsilon - \zeta - f$ RANS model at $Re = 10\,595$ using a grid with 250×10^3 points. The seamless hybrid RANS-LES model is based on the partially integrated transport model (PITM) proposed by Chaouat and Schiestel[77] which is based on adjusting the destruction coefficient $C_{\varepsilon,2}$ in the ε-equation to enable a seamless RANS-LES transition. Chaouat[78] used the PITM approach within a second-moment closure model for a simulation of the hill flow at $Re = 10\,595$ on a finer grid with 10^6 points.

Balakumar *et al.*[6] performed DNS, LES, and wall-modeled LES of this flow at $Re = 10\,595$. DNS and LES were performed with a high-order structured code using meshes with 200 and 5.5×10^6 cells, respectively. The wall-modeled LES calculations were carried out by a second-order unstructured finite volume code using a mesh with 1.2×10^6 cells.

C. Previous studies: High Reynolds number

Experimental studies of this flow at a higher Reynolds number of $Re = 37\,000$ have been carried out by Rapp and Manhart.[79] A water channel of eleven meters in length has been used in the Hydromechanik Laboratorium of the Technische Universität München. Hills having a height of $3.035h$ were installed in the rectangular channel (dimensions are given in terms of the hill height $h = 50$ mm). The width of channel was chosen to be $18h$ to achieve homogeneity in spanwise direction. Ten hills with an inter-hill distance of $9h$ were installed inside the channel. Two-dimensional particle image velocimetry (PIV) and laser-Doppler anemometry (LDA) were used as measurement techniques. Based on an analysis of the results (including two point correlations), the authors concluded that the assumptions of streamwise periodicity (after ≈6–8 hills) and spanwise homogeneity (for about $10h$ in the center of the set-up) are valid and that the streamwise velocity fluctuations become uncorrelated in spanwise direction at $z \approx 4h$ for moderate and high Reynolds numbers $Re \geq 10\,600$. The mean velocity and turbulent stresses in different sections of the channel are available as a ERCOFTAC database.[80]

Numerical simulations of this flow at $Re = 37\,000$ have been performed by Chaouat and Schiestel.[81] They applied their PITM hybrid model[77] on grids ranging from 240×10^3 to 960×10^3 points. PITM simulation results were compared with RANS Reynolds stress model (RSM) results. The authors observed that in contrast to the PITM simulations, the RSM computations showed important weaknesses regarding the prediction of this flow caused by the lack of large unsteady eddies.

IV. LES SIMULATION SETUP

The numerical realization of LES is described next. First, we describe the setup of simulations. Then, the LES resolution is evaluated based on different criteria.

A. Simulation setup

Figure 3 shows the computational domain applied in our simulations. The size of the computational domain is $L_x = 9h$, $L_y = 3.035h$, and $L_z = 4.5h$ in streamwise (x), wall normal (y), and

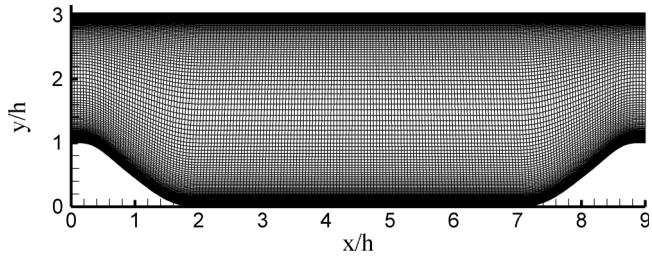

FIG. 3. Computational domain of two-dimensional hill flow simulations: A sample curvilinear grid is shown.

spanwise (z) directions, respectively, where h is the height of the hill. The hill crest is located at $(x, y)/h = (0, 1)$. The Reynolds number $Re = U_b h/\nu$ is $Re = 37\,000$ based on the hill height and bulk velocity above the hill crest at $x = 0$. At the bottom and top, the channel is constrained by solid walls. No-slip and impermeability boundary conditions are used at these walls. Periodic boundary conditions are employed in streamwise and spanwise directions.

The computations are initialized in two ways. Using the coarse grid, the flow is initialized by a uniform bulk velocity U_b, whereas on fine grids the flow field is initialized by interpolating flow field results obtained on a coarse grid. Throughout the paper, h and U_b are used as reference quantities for a length and velocity. All data presented are made dimensionless with these quantities. After 20 flow-through times, mean quantities were averaged over 140 flow-through times and averaged in the spanwise direction. The time step was chosen to imply a maximum CFL number of 0.5 and an averaged CFL number of about 0.1.

B. LES flow resolution: Grid requirements

Pure dynamic LES is used below to evaluate the performance of our DLUM hybrid RANS-LES method. In this regard, a very important question is the characterization of the ability of pure dynamic LES to resolve the flow.

To address this question we considered three grid configurations of performing LES simulations. Table I summarizes these grid configurations and their resolution in wall units: we consider fine (20M), medium (5M), and coarse (500K) grids which contain 20, 5, 0.5×10^6 cells, respectively. The medium grid is similar to the grid used by Fröhlich *et al.*[72] in their study of this flow at $Re = 10\,595$. The fine grid is obtained by refining the grid in x, y, and z direction using the same proportion. The coarse grid is obtained by coarsening the medium grid in all three directions, but first of all in the spanwise direction.

The well-resolved LES grid resolution criteria for attached flows estimated by Piomelli and Chasnov[82] require $\Delta x^+ \approx 50$, $y^+ \approx 1$, and $\Delta z^+ \approx 15$. The grid resolution of the fine grid satisfies the grid resolution recommendation of Piomelli and Chasnov in y direction, but the resolution is insufficient in the spanwise and streamwise directions. To strictly satisfy the LES grid resolution requirements we would have to double the number of grid points in the streamwise direction, and to triple the number of grid points in the spanwise direction. Correspondingly, we would need about 120×10^6 grid cells to enable wall-resolved LES simulations according to the criteria suggested by Piomelli and Chasnov.[82] Given our computational resources, this turned out to be infeasible.

TABLE I. Grid configurations and resolution parameters for fine, medium, and coarse LES.

Grid	N_{cell}	$N_x \times N_y \times N_z$	y^+_{avg}	Δx^+_{max}	Δz^+_{max}
20M grid	20M	$350 \times 170 \times 348$	0.5	115	58
5M grid	5M	$200 \times 130 \times 190$	1	210	110
500K grid	500K	$128 \times 80 \times 48$	2	295	390

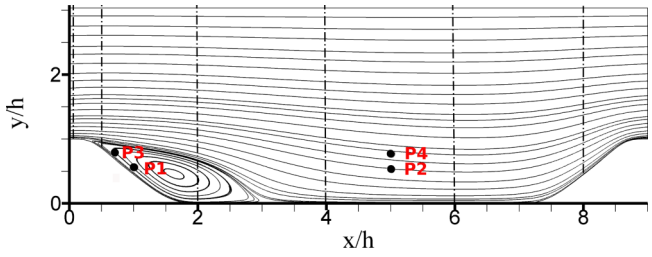

FIG. 4. Schematic plot showing the position of four points in the mid-span xy plane where velocity two-point correlation functions were calculated. The points P1 and P3 with coordinates $(x, y)/h = (1, 0.6)$ and $(x, y)/h = (0.65, 0.8)$ are located inside the recirculation bubble. The points P2 and P4 with coordinates $(x, y)/h = (5, 0.6)$ and $(x, y)/h = (5, 0.8)$ serve as corresponding reference points. The vertical dashed lines show the positions where LES and DLUM profiles are compared (see Sec. VI).

C. LES flow resolution: Correlation functions

By analyzing criteria for the assessment of the LES flow resolution, Davidson[83,84] concluded that the calculation of velocity two-point correlations represents the most reliable approach to determine the LES flow resolution. We performed such two-point correlation calculations to evaluate the resolution of our LES. The correlation function calculations were performed after the flow reached a stationary state by using 16 000 independent samples. Independent samples were obtained by using a temporal window between different samples. The time period, $L_x/(3U_b)$, of this temporal window corresponds approximately to the time needed for the fluid to pass one third of the computational domain. By further increasing this time interval, we have not seen relevant differences in the results. We calculated correlation functions at four points. Figure 4 illustrates their location in the flow field. Two points are located inside the recirculation bubble, and the other two points, which serve as reference points outside the recirculation bubble, are in the recovery region.

Figure 5 shows snapshots of streamwise turbulent velocity fluctuations. The location of the points P1, P2, P3, and P4 is indicated in these figures. Figure 6 presents the corresponding streamwise two-point correlation $R_{uu}(x - x_0) = \langle u(x_0)u(x)\rangle$ normalized by u^2_{rms} along the x axis for the three LES grids considered (500K, 5M, and 20M) at the given locations. Markers on the lines show the correlation function values at specific grid points to clearly specify the resolution for each grid. The two point correlations, R_{vv} and R_{ww}, are similar for the three grids considered. Therefore, they are not shown here.

Let us look first at the features at the reference points, P2 and P4, outside the recirculation bubble. We see that the two-point correlations for all the grids considered are similar. The only noticeable difference is given at P4 by using the coarse grid. The point P4 is located near the shear layer. The agreement of correlation functions obtained on the fine and medium grids indicates

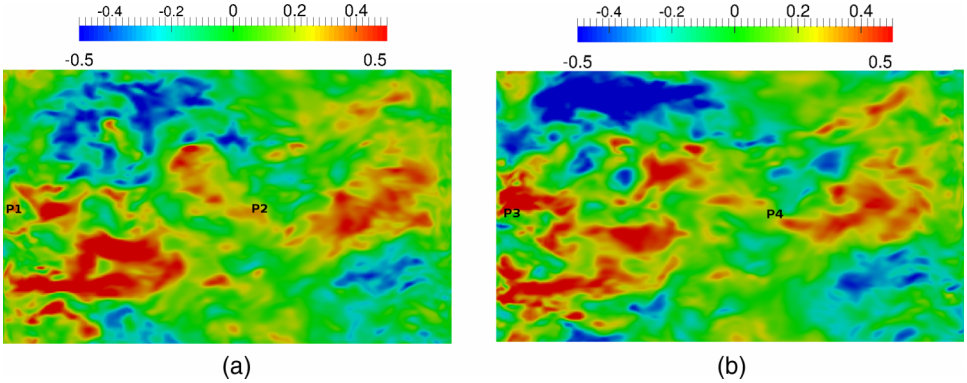

FIG. 5. Snapshots of streamwise velocity fluctuations in the xz plane involving P1, P2, P3, and P4 (see Fig. 4). (a) Plot involving P1 and P2. (b) Plot involving P3 and P4.

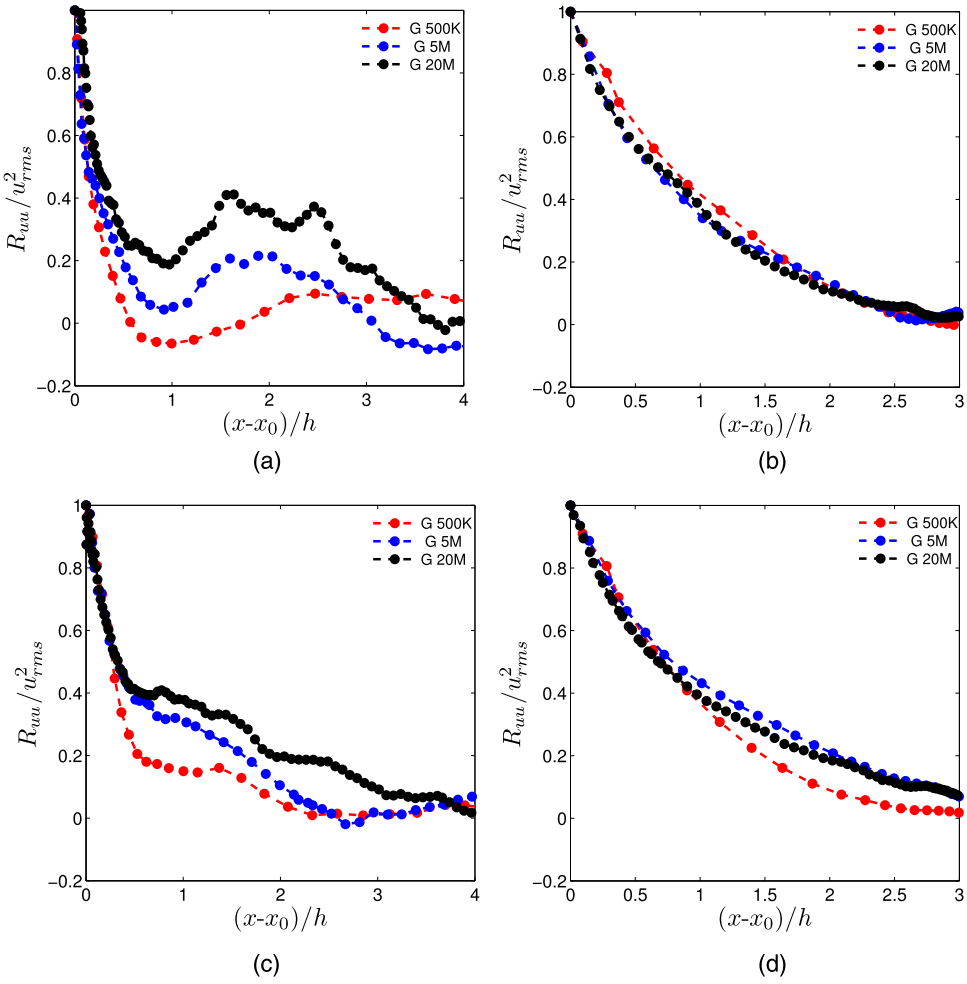

FIG. 6. Comparison of normalized streamwise velocity two-point correlations for three grid configurations at four locations obtained from pure LES. Markers on the lines indicate the resolution of each grid (every third symbol is shown). (a) At position P1. (b) At position P2. (c) At position P3. (d) At position P4.

that both these grids are sufficiently fine. However, the coarse grid correlation function decays too quickly, showing that the coarse grid is slightly too coarse to appropriately resolve the turbulence structures in the shear layer.

The features at P1 and P3 inside the recirculation bubble are different. Figure 5 illustrates the coherent structure of the recirculation bubble by extended areas of positive fluctuations (corresponding to turbulence flowing along the x axis) and negative fluctuations (corresponding to turbulence flowing in the opposite direction). It may be also seen that this coherent structure is even more pronounced at the higher P3 than at P1. The shape of correlation functions is clearly affected by the recirculation bubble. A significant amount of small scale (decorrelating) turbulence generated by the recirculation bubble implies that the correlation decays much faster than seen at the reference points P2 and P4. In contrast to the features seen at the reference points P2 and P4, we see at P1, where we have clearly pronounced coherent structures (see Fig. 5), a correlation increase after the rapid initial correlation decay. The latter correlation increase is the effect of correlations generated by the coherent recirculation bubble.

Figures 6(a) and 6(c) can be used to derive the following conclusions regarding the resolution ability of the three LESs considered. According to Davidson's analysis,[83,84] significant differences cannot be expected. With respect to the (20M, 5M, 500K) grids considered, the correlation functions shown in Fig. 6 involve about (170, 90, 60) grid points at P1 and (200, 110, 75) grid points at P3, respectively. The rapid decay of correlation functions from 1 to 0.5 is resolved by (30, 15, 10)

grid points at P1 and (50, 30, 20) grid points at P3, respectively. This is expected to be sufficient for a reasonable flow resolution.[83,84] What we see, however, are significant differences of correlation functions in Figs. 6(a) and 6(c) depending on the grid applied. It appears that all three grids are capable of reasonably well resolving the rapid short-range correlation decay. Differences between correlation functions can be seen with respect to their ability to reflect the large-scale spatial organisation of the recirculation bubble. The correlation functions for $1 \leq (x - x_0/h) \leq 2.5$ confirm the expectation that a grid coarsening reduces long-range correlations of velocities: the filtering of velocities over a larger spatial domain implied by the grid coarsening represents a decorrelating effect. The significant differences between the 5M and 20M grid results support the view that the 20M grid still does not enable fully resolved LES, i.e., it still implies under-resolved LES. Therefore, we refer to our 20M LES grid as the fine grid LES rather than the well resolved LES. The difference of our conclusions to the grid-point based arguments of Davidson[83,84] can be explained by the different structure of correlation functions considered. In particular, the correlation function shapes analyzed by Davidson are basically equivalent to the correlation functions seen at the reference points P2 and P4 here, this means Davidson considered correlation functions that are not affected by long-range correlations as seen in the correlation functions at P1 and P3.

V. DLUM SIMULATION SETUP

The next step is the completion and discussion of the numerical setup of our new hybrid RANS-LES method. One ingredient, which was not discussed so far, is the reflection of the wall damping effect if the model is in RANS mode. After addressing this issue, we consider the suitability of several grids to perform hybrid RANS-LES simulations and the effect of variations of the definition of the LES filter width. Finally, the treatment of the RANS-LES transition region defined in this way is discussed.

A. Damping function

The calculation of the coefficient C_μ in the turbulent viscosity $\nu_t = C_\mu k/\omega$ in RANS mode, which was postponed in Sec. II C, is addressed next. A correct reflection of wall damping effects is known to require a decreasing C_μ value with decreasing wall distance.[85] We addressed this problem by focusing on two relevant features. First, the damping function model should not involve any geometrical wall distance, which would make applications to turbulent flows in complex geometries (flow along a right angled corner) very difficult. Second, the damping function model should involve parameters that enable its appropriate use in a hybrid RANS-LES method. In particular the second criterion represents a challenging problem because damping function concepts used in the RANS context do not need to work well in hybrid RANS-LES methods (characteristic turbulence velocity and time scales which are modeled in hybrid RANS-LES methods can be much smaller compared to the RANS case—this can lead to the simulation of wall damping effects in flow regions that are actually not affected by wall damping). After analyzing several options we decided to follow concepts of the elliptic blending approach.[86–89] As shown below, this approach is capable of dealing well with the two criteria described above.

Within this approach, C_μ is assumed to be given by $C_\mu = (1 - f_\alpha)C_\mu^w + f_\alpha C_\mu^\infty$. Here, f_α is a blending function, and C_μ^w and C_μ^∞ are characteristic values of C_μ that reflect C_μ at the wall and C_μ far away from the wall, respectively. We use $C_\mu^{wall} = 0$, $C_\mu^\infty = 0.09$, and $f_\alpha = \alpha^3$, such that the C_μ relation reduces to

$$C_\mu = 0.09\alpha^3. \tag{15}$$

The variable α defines the closeness to a solid wall. It satisfies the elliptic equation[88,89]

$$\alpha - L_d^2 \nabla^2 \alpha = 1 \tag{16}$$

with the boundary condition $\alpha = 0$ at the walls. The way in which α varies with L_d can be seen in terms of Fig. 7, which was obtained by using the DLUM on the 500K grid. This figure shows

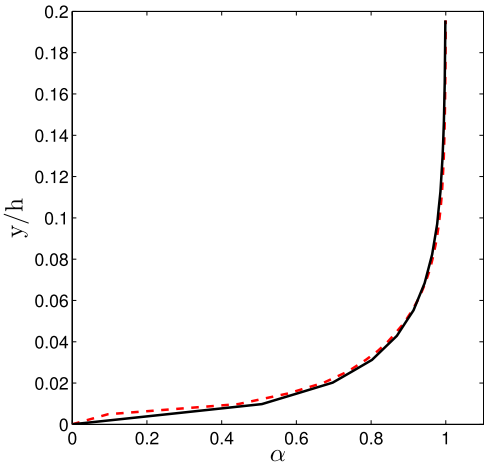

FIG. 7. The wall distance parameter α (see Sec. V A) obtained by the DLUM at $x/h = 6$: DLUM result (black solid line) and $\alpha = 1 - exp(-1.25y/L_d)$ (red dashed line).

that α can be approximated very well by $\alpha = 1 - exp(-1.25y/L_d)$ in the region close to the lower wall. This variation is plausible. For a constant L_d corresponding to homogeneous turbulence, the solution to α in Eq. (16) would be given by $\alpha = 1 - exp(-y/L_d)$. Hence, the modification of $\alpha = 1 - exp(-y/L_d)$ by $\alpha = 1 - exp(-1.25y/L_d)$ accounts for the spatial variation of L_d.

In RANS methods, the Durbin limited length scale L_d is given by[85]

$$L_d = max(C_L L, C_\eta \eta). \tag{17}$$

Here, $L = k^{3/2}/\epsilon$ is the characteristic length scale of large scale turbulent motions, $\eta = (\nu^3/\epsilon)^{1/4}$ is the Kolmogorov length scale, and $C_L = 0.2$ and $C_\eta = 16$ are used.[90] Using the 250K grid, a pure RANS simulation was performed to illustrate the behavior of C_μ. Figure 8 shows the lateral profiles of α and C_μ at the axial location $x/h = 2$. It can be seen that α and C_μ vanish at the bottom and top walls. The maximum of α approaches the upper limit one as determined by Eq. (16) for the case of vanishing α gradients (i.e., $\nabla^2\alpha = 0$).

However, the use of this concept for hybrid RANS-LES simulations faces questions. One option is to apply Eq. (17) in hybrid RANS-LES simulations. This method is referred to as DLUM-NW (NW refers to the near wall DLUM version). Figure 9 reveals the problem of this approach. Used in a hybrid method, the characteristic turbulence length scales $C_L L$ and $C_\eta \eta$ become much smaller and larger, respectively, compared to the RANS mode (not shown). Correspondingly,

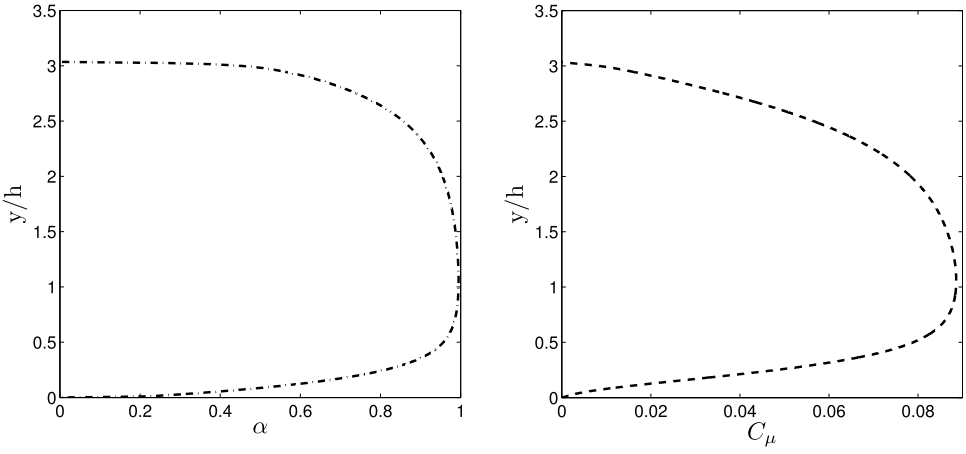

FIG. 8. Profiles of α and C_μ obtained from a pure RANS simulation at an axial location $x/h = 2.0$.

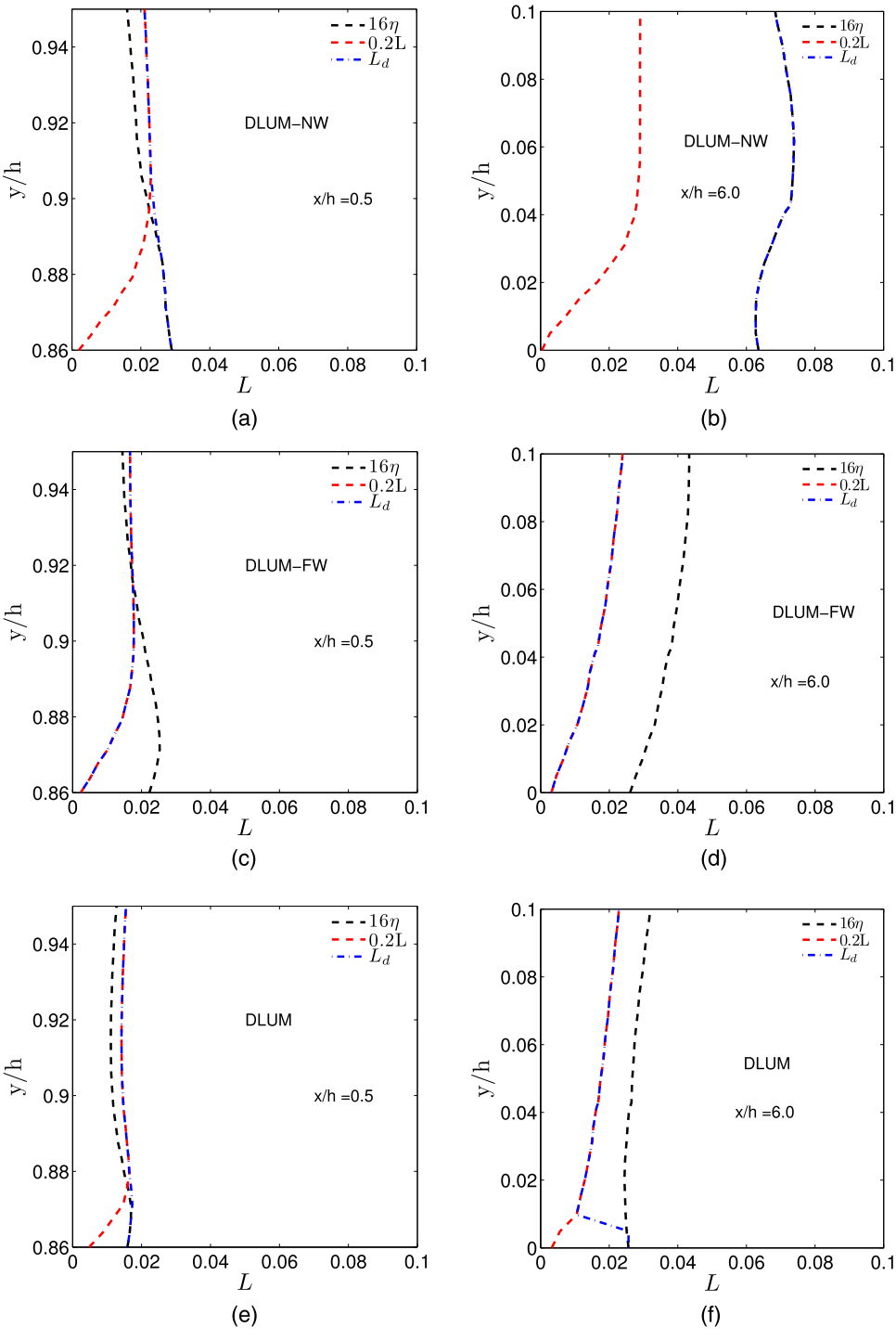

FIG. 9. Characteristic instantaneous length scales L_d, 16η, and $0.2L$ (see Sec. V A) obtained by the DLUM-NW, DLUM-FW, and DLUM at axial locations $x/h = (0.5, 6)$. (a) At $x/h = 0.5$: DLUM-NW. (b) At $x/h = 6$: DLUM-NW. (c) At $x/h = 0.5$: DLUM-FW. (d) At $x/h = 6$: DLUM-FW. (e) At $x/h = 0.5$: DLUM. (f) At $x/h = 6$: DLUM.

L_d may be equal to $C_\eta\eta$ in all the flow fields (see Fig. 9(b)), and $C_\eta\eta$ is found to be bigger than $C_L L$ under these conditions (see Fig. 9). The implications of that can be seen by taking reference to the exponential variation $\alpha = 1 - exp(-1.25\,y/L_d)$ reported above, which implies $\alpha \propto y/L_d$ close to the wall. The use of $L_d = C_\eta\eta$ in this relation, which is relatively high, then leads to small α values

that imply relatively small turbulent viscosities (see Fig. 18). One alternative would be to not apply the Kolmogorov limiter $C_\eta\eta$, this means we have $L_d = C_L L$ everywhere. This method is referred to as DLUM-FW (FW refers to the far-from-the-wall DLUM version). But Fig. 9 indicates that this approach also has significant shortcomings. $L_d = C_L L$ can become very small close to the wall, because it is not bounded by the Kolmogorov limiter. The implications of that can be seen by taking again reference to $\alpha = 1 - exp(-1.25\, y/L_d)$, which implies $\alpha \propto y/L_d$ close to the wall. The use of $L_d = C_L L$ in this relation, which is relatively small, can lead to high α values that imply relatively high turbulent viscosities (see Fig. 18). These indications of shortcomings related to the use of DLUM-NW and DLUM-FW are confirmed below in terms of model applications (see Sec. VI).

The damping function model that we used in our DLUM is a combination of DLUM-NW and DLUM-FM depending on k_{mod}/k_{tot},

$$L_d = \begin{cases} max(C_L L, C_\eta \eta) & \text{if} \quad k_{mod}/k_{tot} > 0.2 \\ C_L L & \text{if} \quad k_{mod}/k_{tot} \le 0.2 \end{cases}. \tag{18}$$

Here, k_{mod}/k_{tot} refers to the ratio of modeled turbulent kinetic energy k_{mod} to the sum k_{tot} of modeled and resolved turbulent kinetic energy. The ratio k_{mod}/k_{tot} was calculated as a time average using the corresponding energy values over the last 70 flow-through times. The motivation for considering Eq. (18) is the idea that the DLUM-NW, which applies $L_d = max(C_L L, C_\eta \eta)$, is used close to the wall (where k_{mod}/k_{tot} is relatively high) and the DLUM-FW, which uses $L_d = C_L L$, is used away from the wall (where k_{mod}/k_{tot} is relatively low). This concept overcomes the DLUM-NW and DLUM-FW problems described above. On the one hand, the DLUM-NW concept is not used under conditions where $L_d = C_\eta \eta$ away from the wall would be a physically inappropriate length scale specification. On the other hand, the DLUM-FW concept is not used close to the wall where $L_d = C_L L$ may imply another inappropriate length scale specification. The use of $k_{mod}/k_{tot} = 0.2$ to separate DLUM-NW and DLUM-FW regimes in Eq. (18) is based on the notion that the characteristic length scale of a regime that is clearly dominated by LES (where $k_{mod}/k_{tot} \le 0.2$) should be L. The use of the DLUM is illustrated in Fig. 9 in comparison to the DLUM-NW and DLUM-FW damping concepts. It may be seen that the DLUM does not suffer from the problematic use of $L_d = C_\eta \eta$ away from walls and $L_d = C_L L$ very close to the wall.

The significant difference between applying damping according to the DLUM and not using any damping is illustrated in Fig. 10 showing hybrid RANS-LES hill flow simulations on the 500K grid. Without using damping, it turns out that mean velocities and Reynolds stress predictions show remarkable shortcomings. Further evidence for the suitability of the DLUM is provided below in Sec. VI.

B. Grid influence

To compare the performance of LES and our new DLUM, we need to decide about the DLUM grid used for such comparisons. To do so, DLUM simulations were performed on several grids by successively refining a grid from 60K cells to 500K cells. Table II summarizes the grids considered. We refer to these grids as 500K, 250K, 120K, and 60K grids.

Figure 11 shows the profiles of the mean streamwise velocity and turbulent shear stress at axial positions $x/h = (2,4)$. It can be seen that the 60K grid is too coarse to provide reasonable results. The 500K and 250K grids are sufficiently fine to obtain very good results. Although the results are grid convergent, we see a minor over-prediction of 500K and 250K DLUM results regarding the turbulent shear stresses. A possible explanation for this observation is that the DLUM behaves similar to LES in the region where we have the maximum turbulent shear stresses (see the averaged turbulent viscosity ratios $\langle \nu_t/\nu \rangle$ in Fig. 18) in conjunction with the fact that the LES is under-resolved, leading to over-predictions of turbulent fluctuations. Given the performance of 500K and 250K grid simulations, we can consider one of these grids to be our standard DLUM grid. Considering the better capturing of the recirculation region, we use the 500K grid as standard grid for the DLUM and LES comparisons reported below.

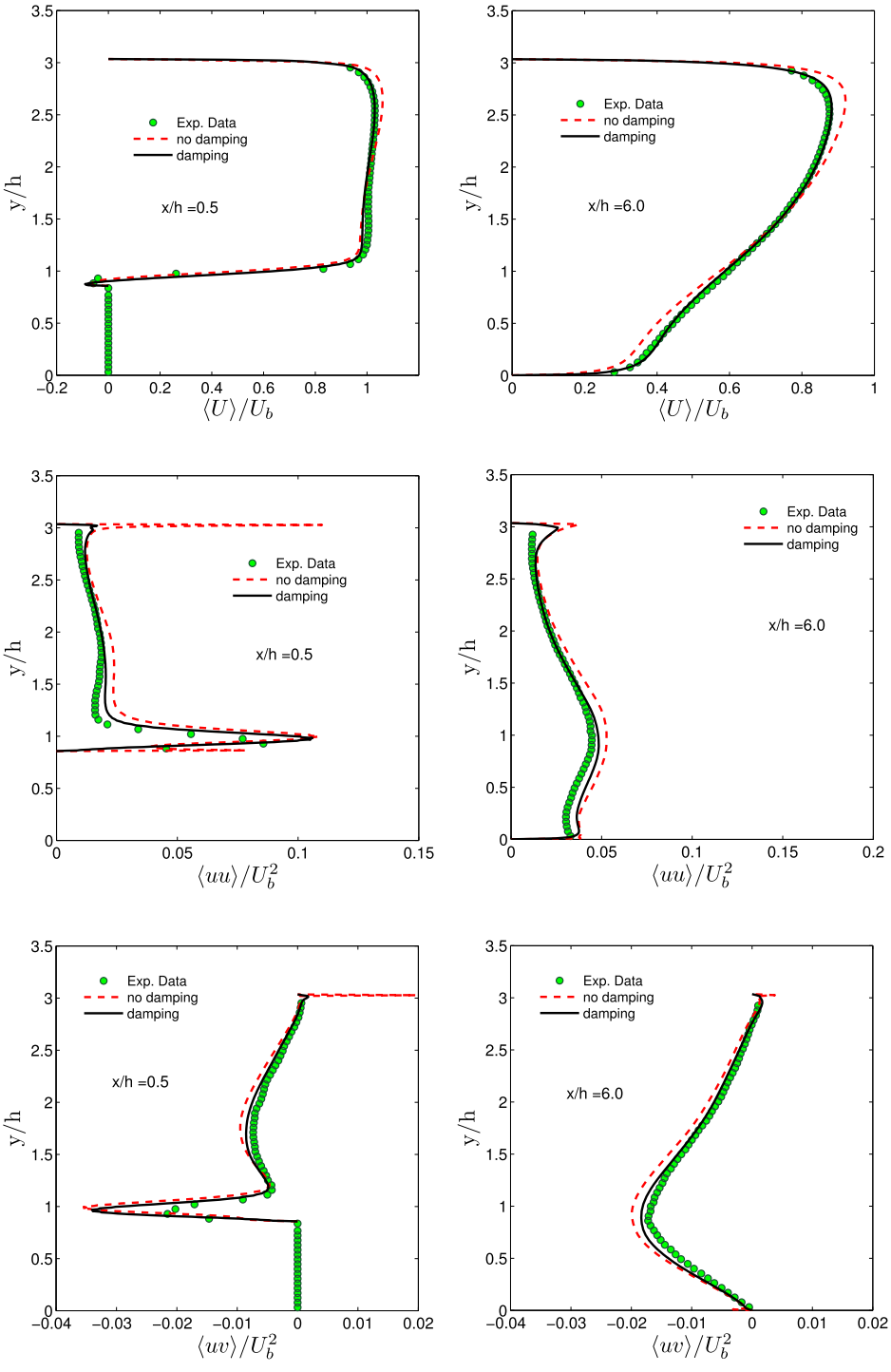

FIG. 10. Effect of damping (see Sec. V A) on predicting profiles of the mean streamwise velocity and Reynolds stresses at axial locations $x/h = (0.5, 6)$.

C. Filter width effect

The filter width Δ applied is known to affect LES results. To evaluate its effect we consider the Δ effect on DLUM simulations. In particular, we compared the effect of $\Delta_{max} = \max(\Delta_x, \Delta_y, \Delta_z)$ that uses the largest side of a cell, which is our standard filter width choice applied in all the other simulations, with the effect of using the volume filter width $\Delta_{vol} = (\Delta_x \Delta_y \Delta_z)^{1/3}$.

TABLE II. Grids used for evaluating the DLUM performance.

Grids	N_{cell}	$N_x \times N_y \times Nz$
500K grid	500K	$128 \times 80 \times 48$
250K grid	250K	$102 \times 64 \times 38$
120K grid	120K	$80 \times 50 \times 30$
60K grid	60K	$63 \times 40 \times 24$

Figure 12 compares DLUM simulation results for the mean streamwise velocity and Reynolds stresses obtained at different axial positions by using the two filter width definitions. Both simulations are performed by using the 500K grid. As can be seen, the use of Δ_{max} gives clearly better results than the use of Δ_{vol}. Similar results are observed with respect to pure LES simulations. Consequently, Δ_{max} is used in all DLUM and pure LES simulation results reported below. It is interesting to note that a recent turbulent channel flow analysis of RANS and LES time scales led to exactly the same conclusion: among four filter width definitions considered, it turned out that the use of Δ_{max} is the most appropriate choice.[45]

D. RANS-LES transition

Let us have a closer look at the RANS-LES transition defined by the DLUM described above. To obtain a quantitative measure for this transition we consider Eq. (12) for τ,

$$\tau = min(\tau^{RANS}, \tau^{LES}) = Tr\tau^{RANS}, \tag{19}$$

where we introduced the transfer function Tr as

$$Tr = min(\tau^{LES}/\tau^{RANS}, 1). \tag{20}$$

Hence, Tr represents a standardized measure for the RANS-LES transition: values smaller than one refer to an LES region, whereas values equal to one refer to a RANS region. By using the definitions $\tau^{RANS} = 1/\omega$ and $\tau^{LES} = \Delta k^{-1/2}$ of time scales we can write Tr also as

$$Tr = min(\Delta k^{-1/2}\omega, 1) = min(\Delta/L, 1), \tag{21}$$

where $L = k^{1/2}/\omega$ refers to the characteristic length scale of large scale turbulent motions. Hence, LES equations are solved for $\Delta < L$, and RANS equations are solved for $\Delta > L$.

Figure 13 shows a snapshot of the transfer function Tr: the RANS region is shown by a red area ($Tr = 1$), and the LES region is shown by a gray area ($Tr < 1$). The RANS layer includes in our simulations a minimum amount of one cell, and a maximum of about 20 cells at different locations. Based on the RANS-LES switch applied, the RANS-LES region fluctuates both in space and time. A further illustration of why we have certain RANS regions can be obtained by looking at the corresponding contours of turbulent length scale L/h in Fig. 13. We see that the length scale L is much smaller in the near wall region than in the outer wall region. According to Eq. (21), Tr switches to RANS mode if $\Delta > L$. We also see that the blue colored length scale distribution is similar to the RANS region in Fig. 13.

It is worth noting that the way of looking at the RANS-LES transition presented here represents one option, which is based on the switch of equation modes. Another way of looking at this problem is to consider the nature of solutions produced by these equations, this means the relative amount of modeled and resolved turbulent kinetic energy. The latter way of addressing the RANS-LES transition question is applied below in conjunction with the discussion of the performance of different models, see Fig. 19.

VI. DLUM VERSUS LES: ACCURACY EVALUATION BY EXPERIMENTS

After describing the computational methods involved we present a comparison of the model performance in simulations. First, we consider streamlines, mean velocity, Reynolds stresses, and

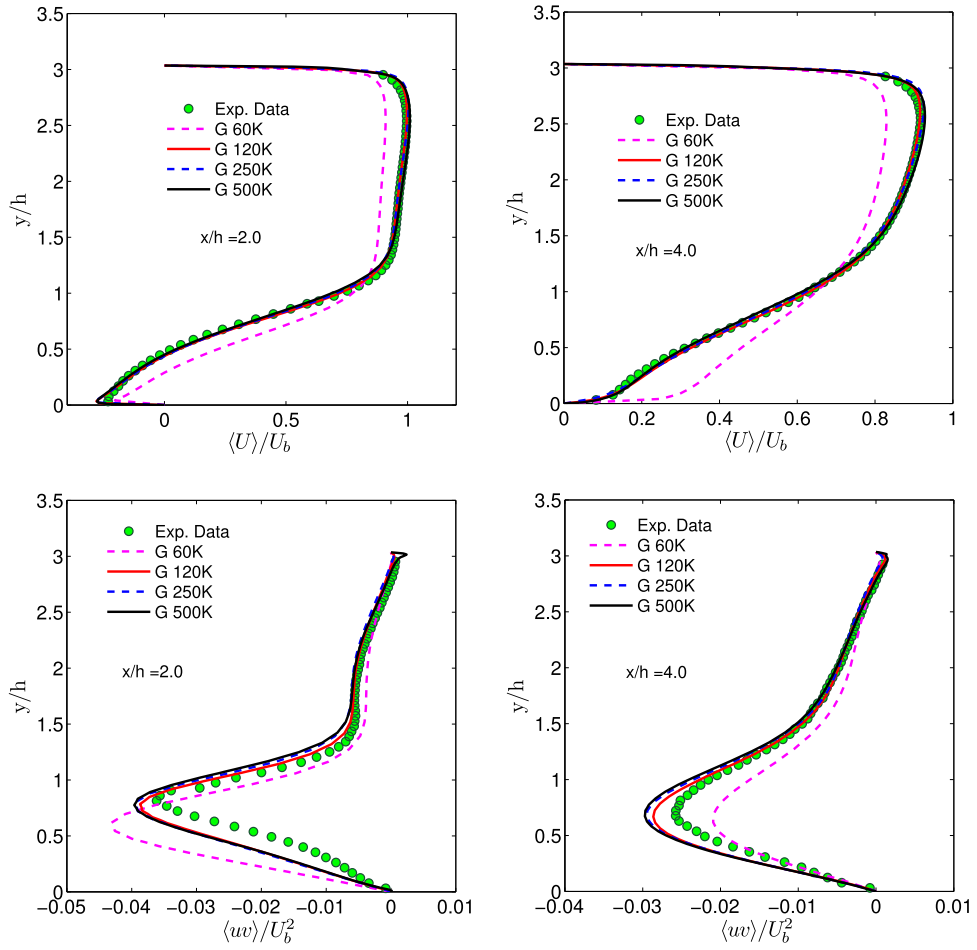

FIG. 11. Grid dependence study of DLUM simulations: Lateral profiles of the mean streamwise velocity and turbulent shear stress at axial locations $x/h = (2, 4)$.

turbulent viscosities on grids introduced above (LES on 20M, 5M, 500K grids, DLUM simulations on the 500K grid). It is worth noting that all LESs considered here are shown to be under-resolved in Sec. IV. Then, LES and DLUM simulations are compared on coarser grids (500K grid simulations are compared with 120K grid simulations).

A. Streamlines

Mean velocity streamlines obtained by LES and DLUM on the three grids are shown in Fig. 14 to give an overview of main flow characteristics. The main focus of the following discussion is on the characterization of the recirculation bubble in terms of separation and reattachment points. The separation point is the point where the velocity direction tangent to the wall surface reverses, which causes the boundary layer to effectively detach from the surface and a recirculating bubble is formed. The reattachment point is the point at which the surface flow reverses after the recirculation bubble. In our numerical simulations, the separation and reattachment points were found using a method that is similar to the method used in the experimental work of Rapp and Manhart.[79] We considered the first two adjacent cells above the wall in separation and reattachment regions where the mean streamwise velocity at the center of these cells changes from negative to positive values. Based on a linear interpolation between the two velocities, we calculated the point of zero velocity. In experiments, the reattachment point is reported as $x/h = 3.76$.[79] The exact separation point is not reported. The accuracy of experimental measurements is reported as one percent.[79]

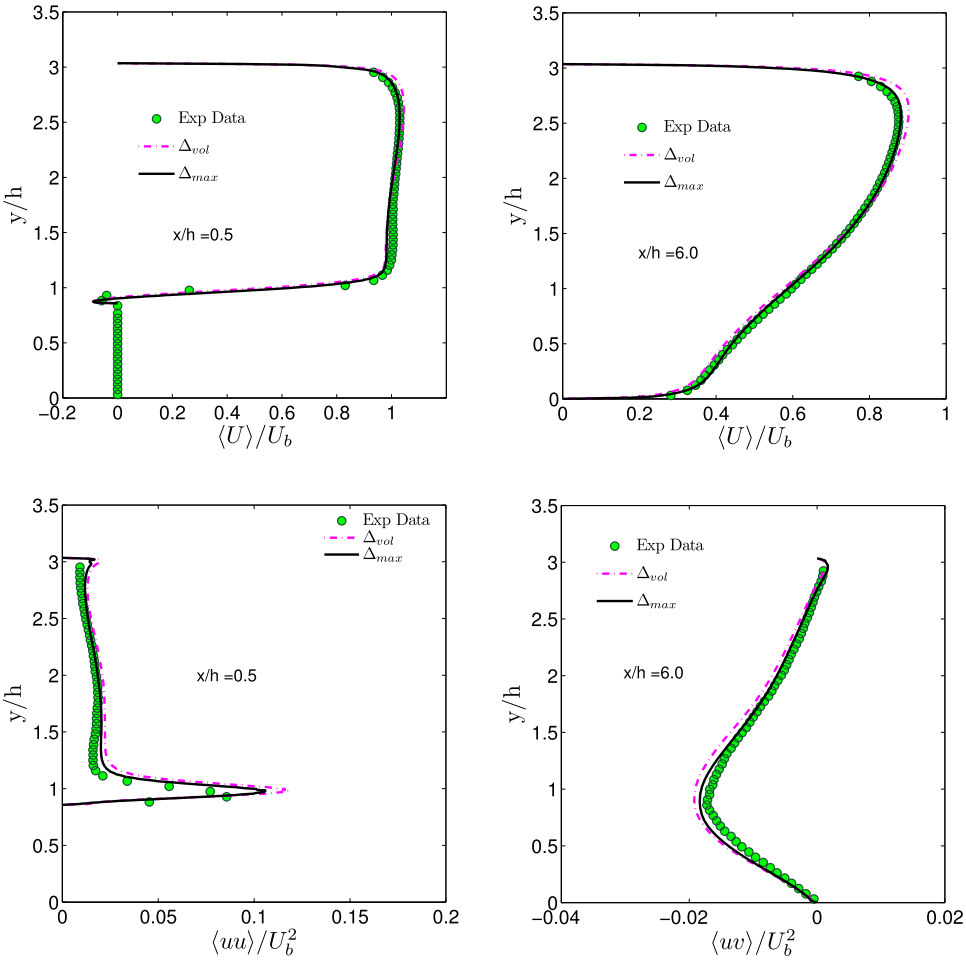

FIG. 12. Mean velocity and Reynolds stress profiles obtained by DLUM simulations using two filter width definitions (see Sec. V C). The profiles are shown at $x/h = (0.5, 6)$.

Table III summarizes the separation, reattachment points, and percentage ϵ_{reatt} of discrepancy with the experimental data for LES and DLUM simulations. The comparison between DLUM and 20M LES results shows that the difference of reattachment and separation points is approximately the same. The difference is that the reattachment point provided by the DLUM is closer to the experimental result than the 20M LES reattachment point. An estimation of the center of the vortex bubble based on the mean velocity streamline plots also shows a corresponding difference between LES and DLUM results: for all LES simulations this center is located at $(x, y)/h \approx (1.7, 0.5)$, whereas the DLUM center is located at $(x, y)/h \approx (2, 0.5)$. There is a difference between fine and

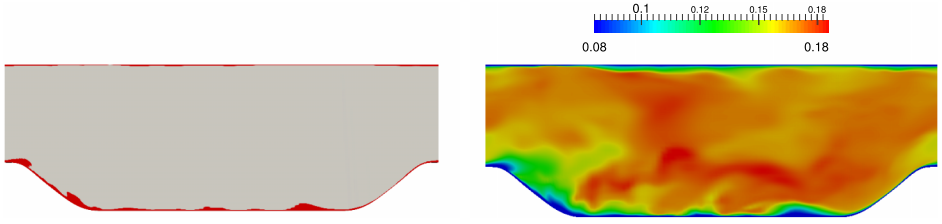

FIG. 13. A snapshot of the RANS layer (left) and turbulent length scale L (right) in the $z = 2.25$ plane. The RANS layer is shown by a red area ($Tr = 1$), and the LES region is shown by a gray area ($Tr < 1$).

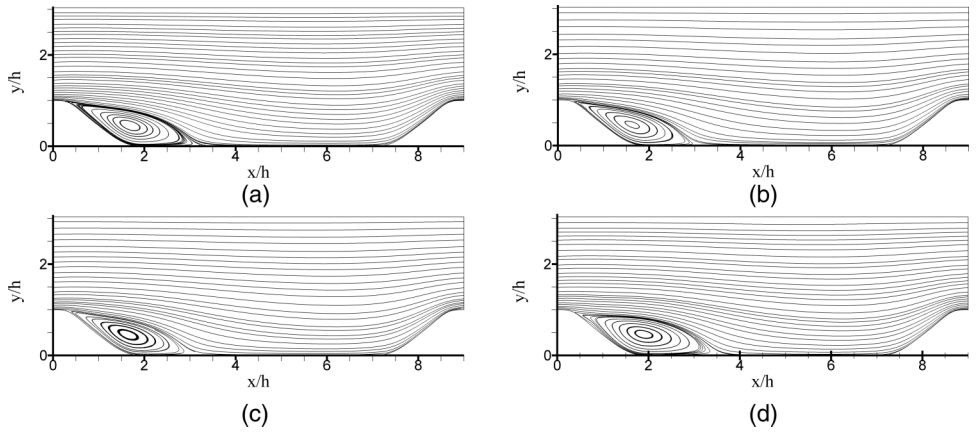

FIG. 14. Streamlines of the mean velocity obtained by LES and DLUM simulations on different grids. (a) LES 20M grid. (b) LES 5M grid. (c) LES 500K grid. (d) DLUM 500K grid.

coarser LES results regarding the difference of reattachment and separation points: the coarser LESs provide this distance 6.4% shorter than the fine grid LES. This indicates shortcomings of coarser LESs to accurately simulate the recirculating bubble. Overall, we conclude that the DLUM performance is better than the performance of the fine grid LES considered.

B. Velocity and Reynolds stresses

Next, the mean streamwise velocity $\langle U\rangle/U_b$ (see Fig. 15), turbulent shear stress $\langle uv\rangle/U_b^2$ (see Fig. 16), and streamwise normal Reynolds stress $\langle uu\rangle/U_b^2$ (see Fig. 17) obtained by the DLUM simulation are compared with the available experimental data[80] and the three LES simulations considered. Here, u and v refer to turbulent fluctuations, and $\langle\cdots\rangle$ refers to Reynolds averaged variables, which were obtained according to the explanations in Sec. IV A. The Reynolds stresses represent the total stresses, i.e., the sum of modeled and resolved parts. The comparisons are presented at six axial locations $x/h = (0.05, 0.5, 2, 4, 6, 8)$: see the illustration in Fig. 4. The selected positions include the regions at the entrance of the channel ($x/h = 0.05$), immediately after separation ($x/h = 0.5$), in the middle of the recirculation bubble close to the leeward hill face ($x/h = 2$), immediately after the reattachment point ($x/h = 4$), after flow recovery ($x/h = 6$), and finally, the acceleration region at the windward slope of the hill ($x/h = 8$).

At the first axial position $x/h = 0.05$, $\langle U\rangle/U_b$ seen in experiments features a near-wall peak due to the first flow acceleration point along the windward of the hill. Both DLUM and LES results slightly underestimate the peak velocity close to the bottom wall, but the DLUM result is much closer to the experimental data. The DLUM result close to the upper wall is in excellent agreement with experimental data, whereas all LES results over-predict $\langle U\rangle/U_b$ in the upper half of the channel for $2 < y/h < 3$. The shear stress $\langle uv\rangle/U_b^2$ shows a discrepancy between experiments, DLUM, and all LES: the computations show a sharp peak in the boundary layer which is absent in experimental data. Possibly, the reason is an insufficient resolution of experimental data. The maximum of

TABLE III. Location of separation and reattachment points obtained by DLUM and LES simulations on different grids.

Simulation	N_{cell}	x/h_{sep}	x/h_{reatt}	ϵ_{reatt} (%)
LES 20M grid	20M	0.23	3.65	3
LES 5M grid	5M	0.24	3.5	7
LES 500K grid	500K	0.3	3.5	7
DLUM 500K grid	500K	0.35	3.8	1

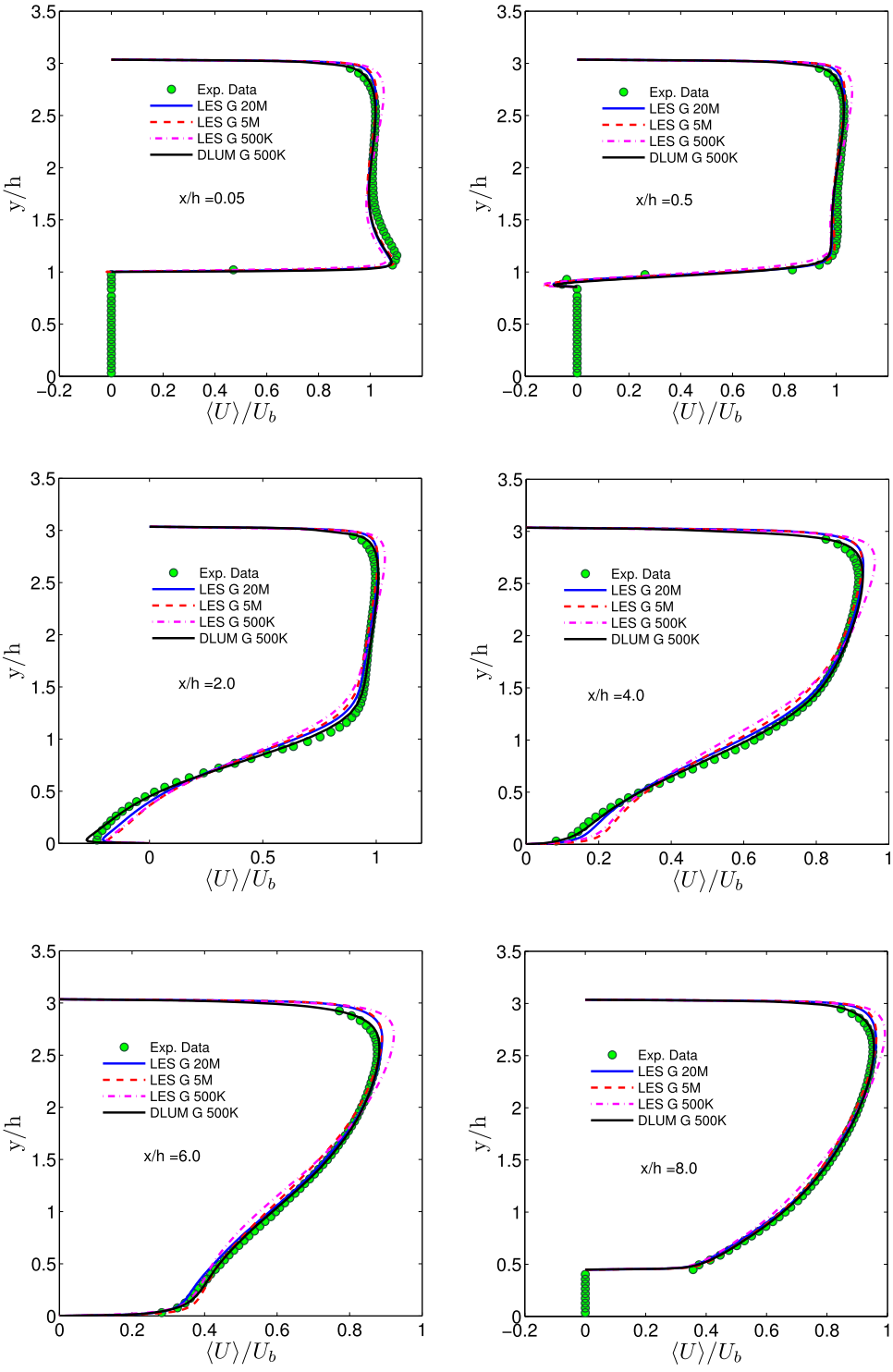

FIG. 15. DLUM versus dynamic LES on different grids and experimental results: Profiles of the streamwise velocity $\langle U\rangle/U_b$ are shown at different axial positions.

$\langle uv\rangle/U_b^2$ in the core of the flow seen in experiments is extremely well reflected by the DLUM. LES results show deficiencies, there is a significant over-prediction of the $\langle uv\rangle/U_b^2$ maximum compared to the experiments. The streamwise normal stress $\langle uu\rangle/U_b^2$ seen in experiments has a substantial peak very close to the lower wall, which is caused by the generation of high shear in the boundary

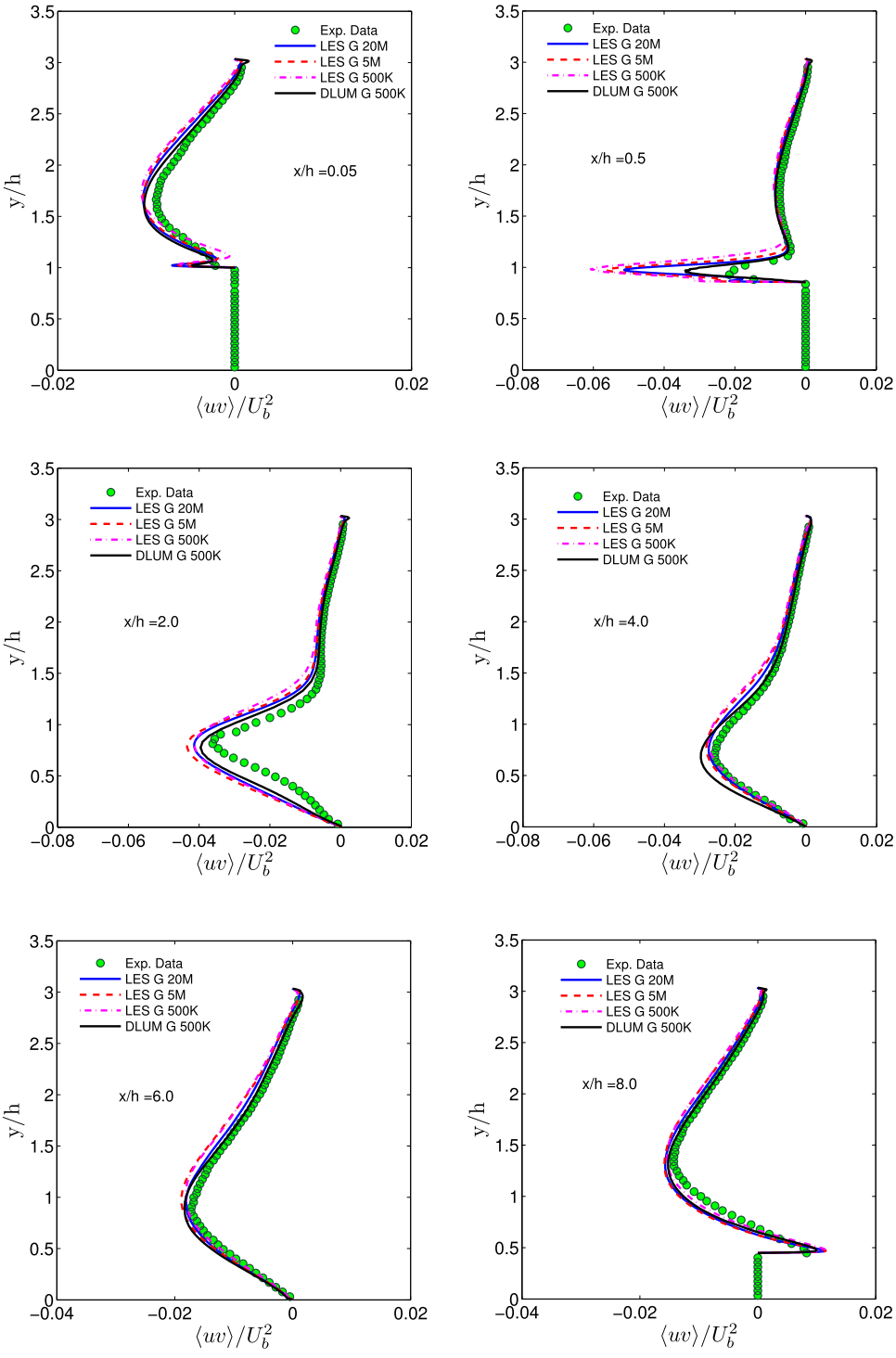

FIG. 16. DLUM versus dynamic LES on different grids and experimental results: Profiles of the turbulent shear stress $\langle uv \rangle / U_b^2$ are shown at different axial positions.

layer. The DLUM slightly over-predicts this peak. Again, this discrepancy may be related to the resolution of experiments. In contrast to the DLUM, all LESs significantly over-predict the lower boundary peak. Above this $\langle uu \rangle / U_b^2$ peak we see an excellent agreement between experiments and DLUM results. Over all of this region, LES results over-predict the experimental results.

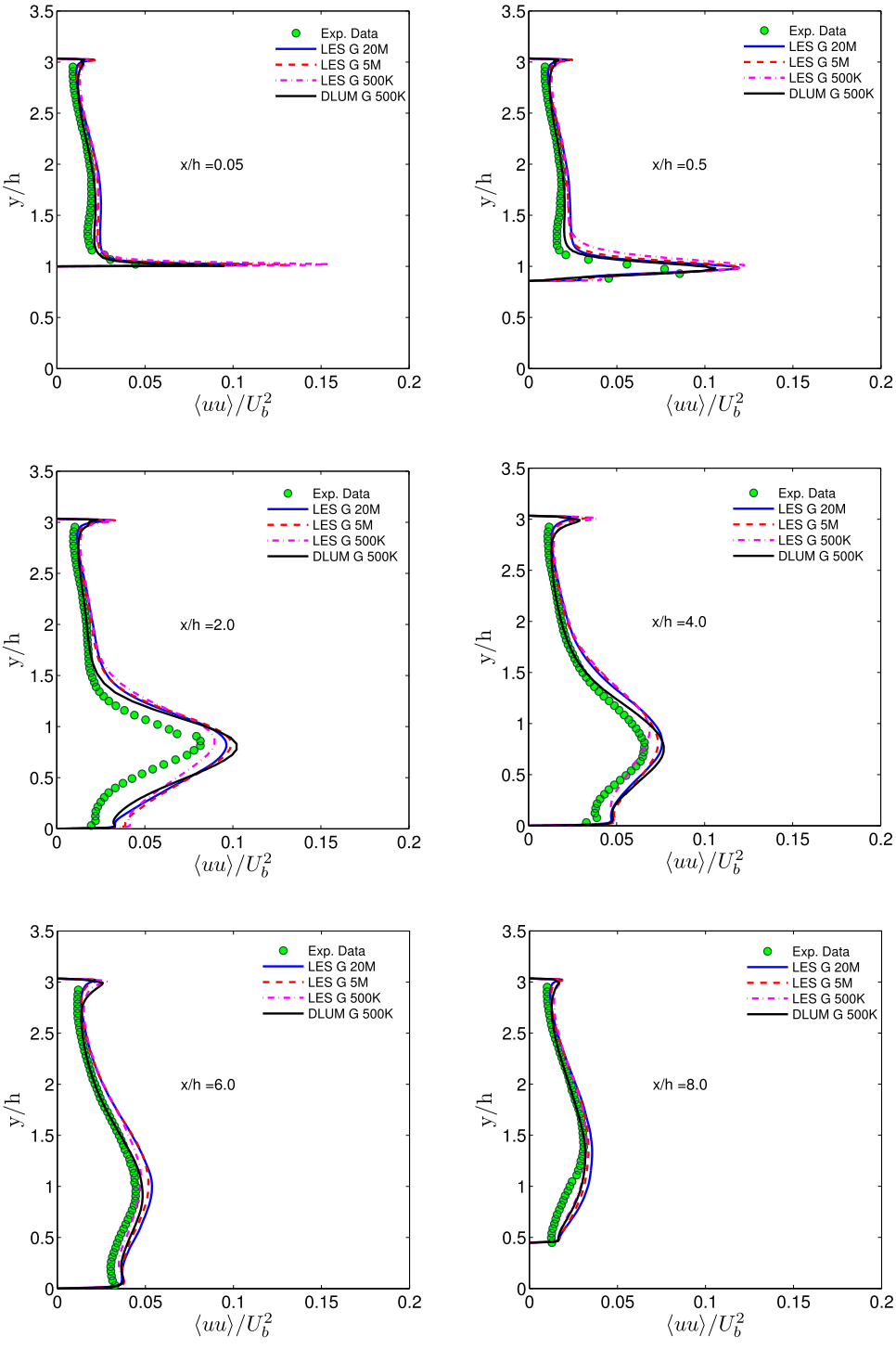

FIG. 17. DLUM versus dynamic LES on different grids and experimental results: Profiles of the normal streamwise Reynolds stress $\langle uu \rangle / U_b^2$ are shown at different axial positions.

At $x/h = 0.5$, immediately after the separation point, $\langle U \rangle / U_b$ seen in the experiments is negative near the wall, this means the boundary layer is detached. All computational methods reflect $\langle U \rangle / U_b$ well in this region. Above the region of negative $\langle U \rangle / U_b$, the DLUM shows an excellent agreement with the experiments. In contrast to the DLUM behavior, $\langle U \rangle / U_b$ is slightly underpredicted by LES in the lower half of the channel ($1 < y/h < 1.5$) and consequently over-predicted

in the upper channel half ($2.5 < y/h < 3$). With respect to the boundary layer peak of the shear stress $\langle uv \rangle / U_b^2$, we see a discrepancy between experiments and the DLUM: the latter over-predicts this peak. There is again the question of whether the experimental results are affected by their resolution. In contrast to the DLUM, all LESs show a significant over-prediction of the boundary layer peak. The peak is reduced by a LES grid refinement, but overall, there is a relatively weak dependence of the peak on the LES grid applied. Above the peak we find a good agreement between experiments and computational results. However, the DLUM performs better than LES compared to the experiments. Regarding the streamwise normal stress $\langle uu \rangle / U_b^2$ we see similar features as $x/h = 0.05$. The near wall $\langle uu \rangle / U_b^2$ peak is spatially more distributed, which reduced the chance to see a resolution effect in the experimental results. It is impressive to see how well the DLUM results agree with the experiments. In contrast to the DLUM, we see an over-prediction of $\langle uu \rangle / U_b^2$ in LES over most of the domain.

The maximum reversed flow occurs at $x/h = 2$, the end of the leeward hill face. This point is in the middle of the recirculation region and therefore of special interest, as it combines three interacting layers: the free shear layer separating from the hill crest, the reversed flow below this layer, and a boundary layer. At this location, there is an almost perfect agreement between DLUM and experimental results for $\langle U \rangle / U_b$. The three LESs considered perform well, but there are discrepancies to the DLUM results (overpredictions of $\langle U \rangle / U_b$ in near-wall regions and a related under-prediction of $\langle U \rangle / U_b$ in the core flow region) that reduce with the grid refinement. The Reynolds stresses, $\langle uv \rangle / U_b^2$ and $\langle uu \rangle / U_b^2$, obtained from computations slightly over-predict the experimental results, but there is a reasonable agreement. Again, the DLUM performs slightly better than LES regarding the reflection of the peaks of $\langle uv \rangle / U_b^2$ and $\langle uu \rangle / U_b^2$.

At the remaining three positions, $x/h = (4, 6, 8)$, the flow physics also changes significantly. In the post-reattachment region at $x/h = 4$, the flow consists of the boundary layer which develops from the reattachment point and the wake that originates from the separated shear layer. In the flow recovery region at $x/h = 6$, halfway between the reattachment and the foot of the next hill, the flow consists of the boundary layer developing from the reattachment point and (above it) a wake which originates from the shear layer further upstream. It is thus characterized by flow components with very different scales and history, which interact to form a flow recovering towards a fully developed flow. At $x/h = 8$, the flow is subjected to strong acceleration. The experimental $\langle U \rangle / U_b$ profiles at these three positions reflect the flow changes, but, on the other side, their basic behavior is not too different. At all these positions, we see again an almost perfect performance of the DLUM with respect to the $\langle U \rangle / U_b$ predictions: there is an excellent agreement with the experiments. The LESs show deficiencies similar to the shortcomings seen at $x/h = 2$. With respect to $\langle uv \rangle / U_b^2$ and $\langle uu \rangle / U_b^2$, the comparison between experimental and computational results leads, basically, to the same conclusions as pointed out for $x/h = 2$. We note that all computational methods are capable of representing the $\langle uv \rangle / U_b^2$ peak well in the boundary layer.

The overall conclusions of these comparisons of velocity and stress profiles can be summarized as follows. The DLUM shows an impressive ability to reflect the most important flow feature, the mean streamwise velocity. The comparisons with experimental data reveal an almost perfect performance of the DLUM. The $\langle uv \rangle / U_b^2$ and $\langle uu \rangle / U_b^2$ profiles predicted by the DLUM are also in very good agreement with experimental results. Minor discrepancies appear in regions affected by high shear, see the profiles at $x/h = (0.05, 0.5)$. A possible reason for these discrepancies may be given by the resolution ability of experiments. Compared to the DLUM, the LES features are different. Significant discrepancies can be seen already in the velocity profiles. The $\langle uv \rangle / U_b^2$ and $\langle uu \rangle / U_b^2$ profiles indicate a trend of LES to over-estimate the experimental results. Reasons for the discrepancies between DLUM and LES features are discussed next.

C. Performance analysis I: LES versus DLUMs

LES and DLUM equations differ in their turbulent viscosities applied. To explain the performance difference between LES and DLUM methods, let us have a look at the profiles of the averaged turbulent viscosity ratio $\langle \nu_t / \nu \rangle$.

A comparison of LES and DLUM turbulent viscosities $\langle \nu_t/\nu \rangle$ is shown in Fig. 18 at the same positions as the mean velocities and Reynolds stresses considered in Sec. VI B. The comparison of the 500K LES with the DLUM using the same grid does clearly show the difference between LES and DLUM: $\langle \nu_t/\nu \rangle$ is approximately the same in the LES-dominated core flow region but the $\langle \nu_t/\nu \rangle$ peaks near the wall seen in DLUM simulations are missing in LES on the same grid. This difference explains the poor performance of the 500K LES compared to the DLUM results. The low viscosity values in LES are related to a high level of turbulent kinetic energy in these regions such that we see the typical features of under-resolved LES: the overprediction of Reynolds stresses and deficiencies seen with respect to mean velocity profiles (see the profiles at $x/h = (0.05, 0.5)$). Compared to the 500K LES, the use of finer LES grids (5M and 20M) reduces the modeled turbulent viscosity. However, the increased production of resolved motions represents an insufficient compensation for that, as may be seen in the LES shear stress profiles shown in Fig. 16.

It is of interest to identify the reason for the advantages of the DLUM compared to LES. Let us address this question first by considering the difference between LES and all three DLUM versions considered. Then, in Sec. VI D, we have a closer look at the differences between DLUM versions. The LES and DLUM versions considered represent viscosity based computational methods that involve a modeled turbulent viscosity. The difference between LES and DLUM versions is the mechanism of how the viscosity is provided in response to a certain flow resolution determined by the computational grid. The DLUM concept implies the desired inherent ability to dynamically adjust the modeled viscosity to the flow resolution: in flow regions of low resolution, it produces higher turbulent viscosities in compensation for the lack of resolved motions. Figure 19, which shows the ratio k_{mod}/k_{tot} of modeled to total kinetic energy for the three DLUM, demonstrates this ability. Close to the wall we have relatively high k_{mod}/k_{tot} ratios, this means areas of relatively low flow resolution. Correspondingly, we find peak values of DLUM turbulent viscosities in these areas: see Fig. 18. This DLUM version ability is a consequence of designing DLUM versions in response to Δ/L variations. High (low) Δ/L values may be considered to correspond to areas of low (high) flow resolution. According to the corresponding use of RANS (LES) modes we have then variations between high RANS (low LES) viscosities, respectively. The LES concept is very different. The modeled viscosity always changes dynamically in response to the intensity of large scale turbulent motions (the dynamic coefficient becomes smaller if a wall weakens the large scale turbulent motions), but the dynamic LES does not have an inherent ability to modify the modeled viscosity in dependence on the flow resolution (no information about the flow resolution enters the dynamic LES equations). This concept does not pose any problems as long as the LES is fully resolving. However, usually this need implies a computational cost that is not affordable. Given a not fully resolving LES, the lack of control of the interaction of modeled and resolved motions may imply insufficient modeled viscosities leading to LES performance deficiencies as observed here.

D. Performance analysis II: DLUM versus DLUM versions

Let us turn now to the differences of the three DLUM versions, which do only differ by their conditioning on the ratio k_{mod}/k_{tot} of modeled to total kinetic energy in the near wall region where the RANS mode is active. In particular, we consider their ability to respond to variations of k_{mod}/k_{tot} with turbulent viscosity changes. By looking again at Fig. 19 we observe that the three DLUM versions imply k_{mod}/k_{tot} variations that take place in a rather thin layer very close to the wall. The turbulent viscosity ratios shown in Fig. 18 respond to k_{mod}/k_{tot} variations: in areas of low resolution (high k_{mod}/k_{tot}) we find relatively high turbulent viscosities.

The differences of DLUM versions are addressed in a more comprehensive way in terms of Fig. 20, which shows contour plots of the turbulent viscosity ratio $\langle \nu_t/\nu \rangle$ and k_{mod}/k_{tot}. Due to the fact that k_{mod}/k_{tot} variations take place in thin layers close to the wall, we do not find extended k_{mod}/k_{tot} variations over all the flow field as given with respect to viscosities. As expected, the largest variations of k_{mod}/k_{tot} take place immediately after separation at about $x/h = 0.5$.

Let us compare first the DLUM-NW and DLUM features. Consistent with the corresponding plots in Fig. 19, the DLUM implies at about $x/h = 0.5$ a more extended area of relatively

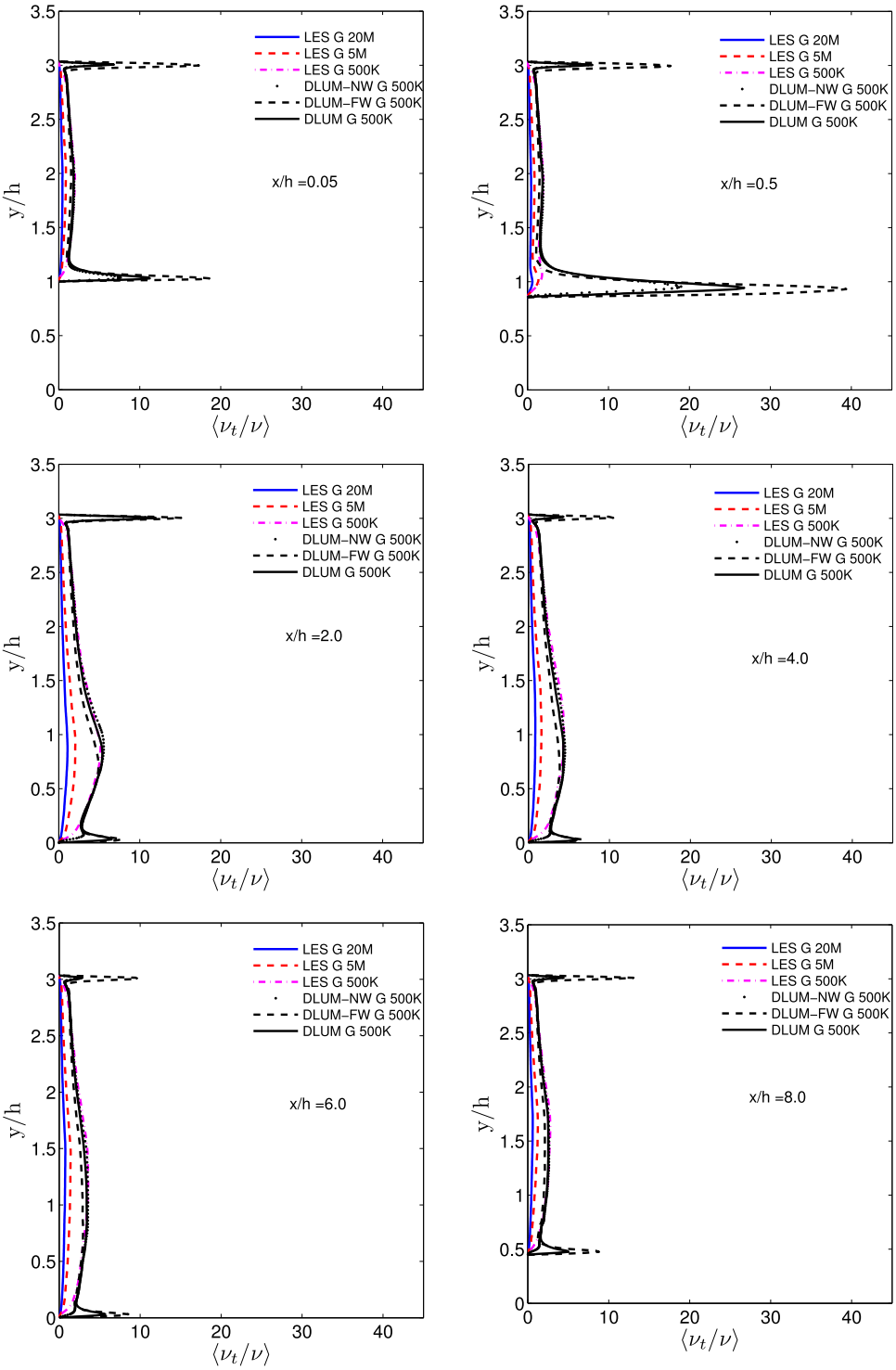

FIG. 18. Profiles of the averaged turbulent viscosity ratio $\langle \nu_t/\nu \rangle$. DLUM results are compared with several dynamic LES and other DLUM version results at different axial positions x/h.

low resolution (high k_{mod}/k_{tot}) compared to the DLUM-NW. It is very interesting to see that the DLUM treats the down-hill near wall region as a less resolved area. The differences of k_{mod}/k_{tot} variations given by the DLUM-NW and DLUM, which may appear to be relatively small, have a clear effect on the turbulent viscosity distributions. In contrast to the DLUM-NW, the

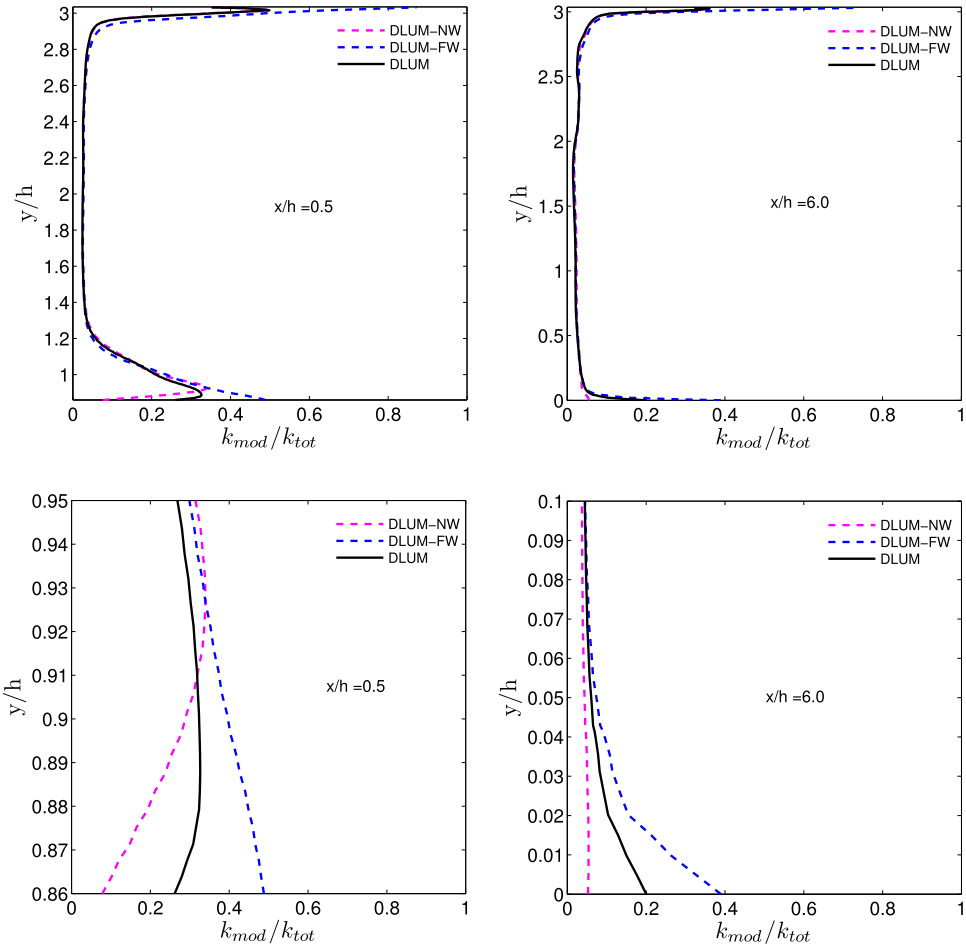

FIG. 19. Profiles of the ratio k_{mod}/k_{tot} of modeled to total turbulent kinetic energy obtained by the three DLUM versions at $x/h = (0.5, 6)$.

DLUM treats the down-hill near wall region in a much more balanced way as an area of relatively low resolution and corresponding high turbulent viscosity. Otherwise, it is relevant to note that the overall viscosity distribution is not affected and basically equal for the DLUM-NW and DLUM.

Next, let us compare the DLUM and DLUM-FW. Compared to the DLUM, the DLUM-FW further extends the areas of relatively low resolution, in particular in the down-hill near wall region. As can be expected, this leads to a further increase of viscosity in the down-hill near wall region. However, the much more dominant effect is a significant change of the overall viscosity distribution. The increased viscosity accumulation near the wall implies a viscosity reduction in most of the other flow: we see larger (blue) areas of relatively small viscosities and smaller (green and red) areas of relatively high viscosities. Compared to the DLUM, neither the imbalanced treatment of the down-hill near wall region implied by the DMUL-NW nor the more imbalanced overall viscosity distribution implied by the DLUM-FW can be expected to contribute to better flow predictions.

It turns out that the differences of DLUM versions discussed in the preceding paragraph imply a different performance in simulations. This is demonstrated in terms of Fig. 21, which shows mean velocities and stresses of DLUM versions in comparison to corresponding pure RANS and LES results on the same grid. First, compared to the DLUM it is surprising to see that the DLUM-NW and DLUM-FW have a relatively limited effect on the stresses. However, there are clear deficiencies of DLUM-NW and DLUM-FW mean velocities. In particular, we see that the DLUM-NW and DLUM-FW produce velocities that are relatively similar to the velocities of pure LES and RANS,

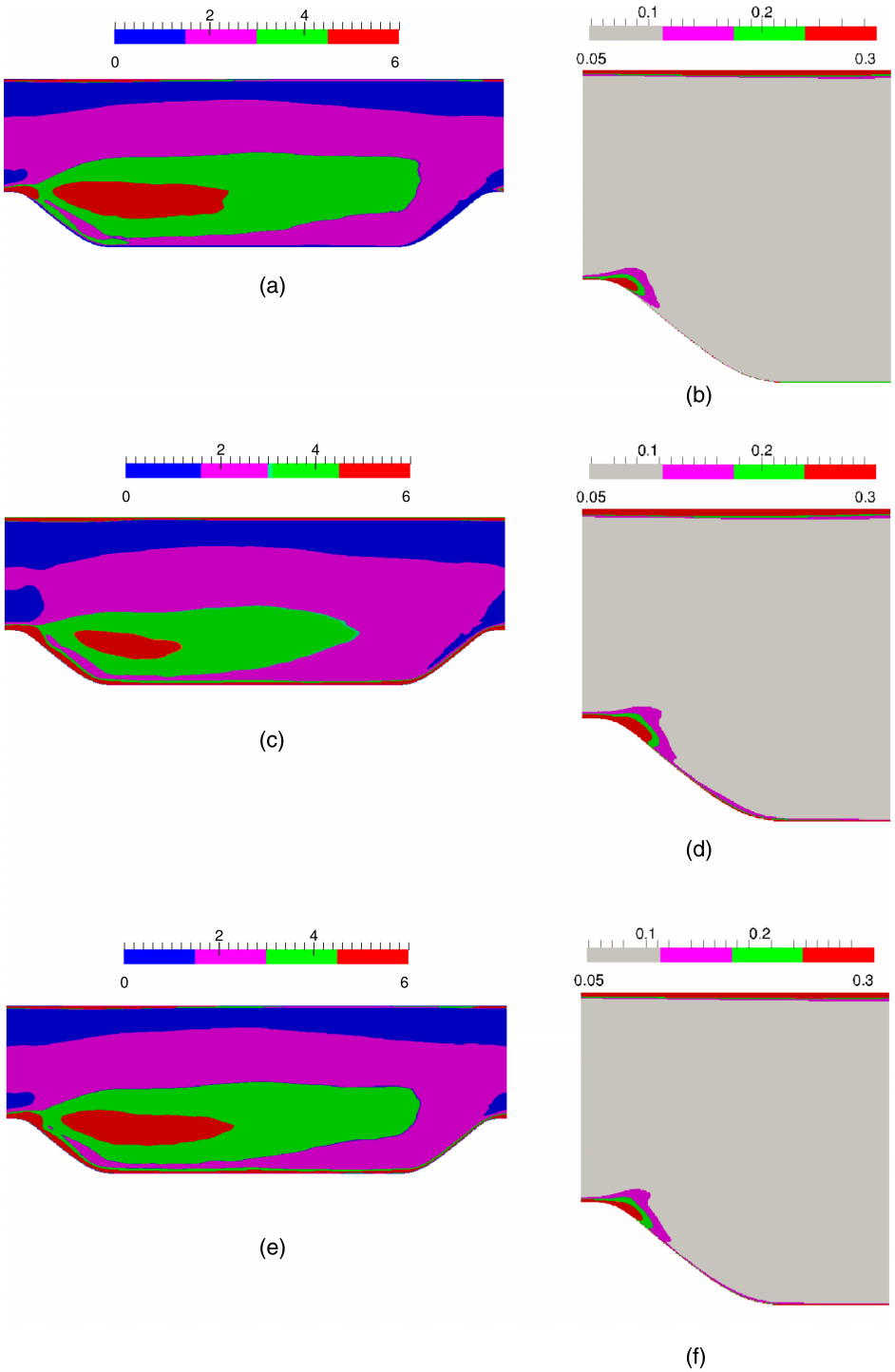

FIG. 20. Comparison of DLUM versions: Contour plots of the turbulent viscosity ratio $\langle \nu_t/\nu \rangle$ (left) and the ratio k_{mod}/k_{tot} of modeled to total turbulent kinetic energy (right) obtained by the three DLUM versions. (a) DLUM-NW. (b) DLUM-NW. (c) DLUM-FW. (d) DLUM-FW. (e) DLUM. (f) DLUM.

respectively. This can be explained by the relatively small and relatively high turbulent viscosities of the DLUM-NW and DLUM-FW, respectively.

The reason for the DLUM-NW and DLUM-FW deficiencies compared to the DLUM can be explained as follows. The significant difference between the DLUM and DLUM-NW and

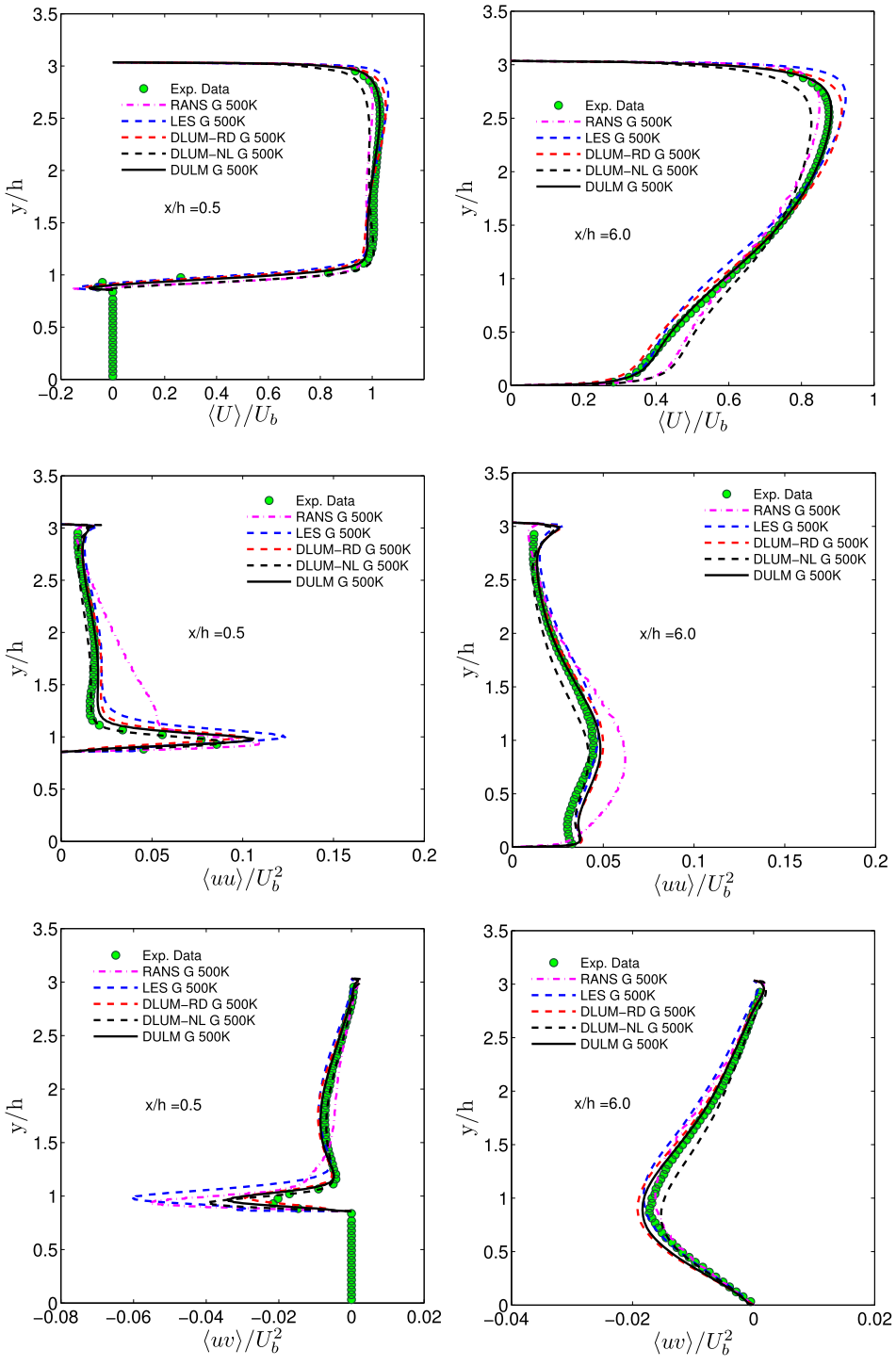

FIG. 21. Comparison of the performance of the three DLUM versions versus RANS, dynamic LES, and experimental data: mean velocities and Reynolds stresses are shown at $x/h = (0.5, 6)$.

DLUM-FW is that the DLUM ensures a physically correct length scale specification, in particular, under the presence of interacting RANS and LES modes (which poses a nontrivial problem, see the discussion in Sec. V A). In combination with the ability to respond with turbulent viscosity variations to resolution changes, the latter requirement appears to be the essential condition to ensure an optimal performance of a hybrid RANS-LES model.

E. Gray area problem

We finish this discussion with a general remark on the difference between the DLUM and other hybrid RANS-LES methods. The gray area problem is often seen to be the most challenging problem of developing hybrid RANS-LES methods. The gray area refers to the transition zone of regions that are treated as RANS and LES, this means the zone where we have difficulties to explain which type of simulation is actually applied. The term gray area problem refers to problems arising from the treatment of this transition zone. In particular, we may see a lack of fluctuations in the entrance region of LES-dominated regions, leading to a decreased ability of LES to resolve motions. Or, we may see an excess of fluctuations in RANS-dominated regions, leading to performance shortcomings because RANS equations are not designed to deal with a significant amount of fluctuations.

The DLUM results reported here do not give any indication of a gray area problem related to the DLUM. The same applies if this problem is considered from a theoretical view point. The DLUM can be seen as dynamic LES where RANS is used to dynamically adjust the turbulent viscosity to a changing flow resolution. In this way, LES and RANS are not used as independent computational methods that need to be merged. Therefore, there is no reason to expect a gray zone problem because a gray zone does not exist.

The gray area problem is usually addressed by asking whether the hybrid RANS-LES model considered implies a log-law mismatch, this means significant deviations from the log-law mean velocity profile, see, e.g., Ref. 45. To provide further evidence for the view presented in the preceding paragraph, we consider the mean velocity profile close to the wall. Due to the presence of the recirculation region, there is no log-law-like behavior of the mean velocity close to the lower wall. Characteristic mean velocity variations close to the upper wall are shown in wall-units at $x/h = (0.5, 6)$ in Fig. 22 by including the log-law indicator function $I = dU^+/dln(y^+)$. It may be seen that there are significant differences between the DLUM predictions and the corresponding behavior seen in channel flow without hills: the typical $U^+ = y^+$ variation in the viscous layer is missing, and U^+ is much higher than seen in regular channel flow. These differences can be attributed to the DLUM grid resolution and the hill-induced high velocity values in the upper half of channel flow here, see Fig. 15, respectively. In particular for $x/h = 6$, the log-law indicator function indicates a log-law-like mean velocity variation close to the wall. Unfortunately, experimental data are missing in this flow region. However, the most important observation is the following: a log-law mismatch produced by any hybrid RANS-LES model is always also seen by a significant velocity over-prediction in the defect layer, but in this flow region we see an excellent agreement between

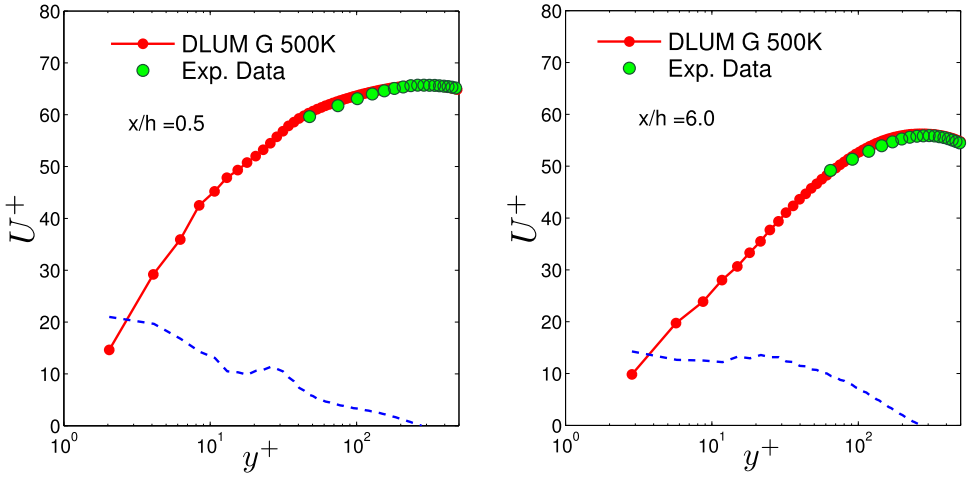

FIG. 22. Mean velocity U^+ in wall-units versus $ln(y^+)$: Comparison of DLUM results and experimental data at $x/h = (0.5, 6)$. Here, y^+ refers to the distance to the upper wall in wall-units. The blue line shows the log-law indicator function $I = dU^+/dln(y^+)$.

DLUM results and experimental data. Thus, this comparison does also support the view that the DLUM does not suffer from the gray area problem.

F. Very coarse grid simulations

Simulations of real engineering flows often face the need to require a huge number of grid points. For example, a pure LES of a realistic flow over an aircraft would need more than 10^{11} cells.[91] Although hybrid RANS-LES simulations are computationally much more efficient, such a realistic aircraft flow simulation would still require approximately 10^8 cells. The only alternative is then often to perform simulations on relatively coarse grids. In this regard, the question of how a grid coarsening affects the performance of computational methods is very important. Given that a coarse grid cannot be expected to provide extremely accurate results, we focus the discussion of this question on the most important flow characteristics, the mean velocity.

We addressed this question in terms of Fig. 23, which shows the profiles of the streamwise velocity obtained by LES and DLUM simulations at four axial locations $x/h = (1,2,3,4)$ for two grids: the 500K grid involved already in the comparisons presented in Secs. VI A-VI C, and a much coarser 120K grid. First, we see that the LES results presented are rather sensitive to the grid resolution. The use of the 120K grid further contributes to increasing discrepancies between LES and experimental results. Second, the most impressive result is that the mean velocity obtained by the DLUM is hardly affected by this grid coarsening, there is hardly any noticeable difference between

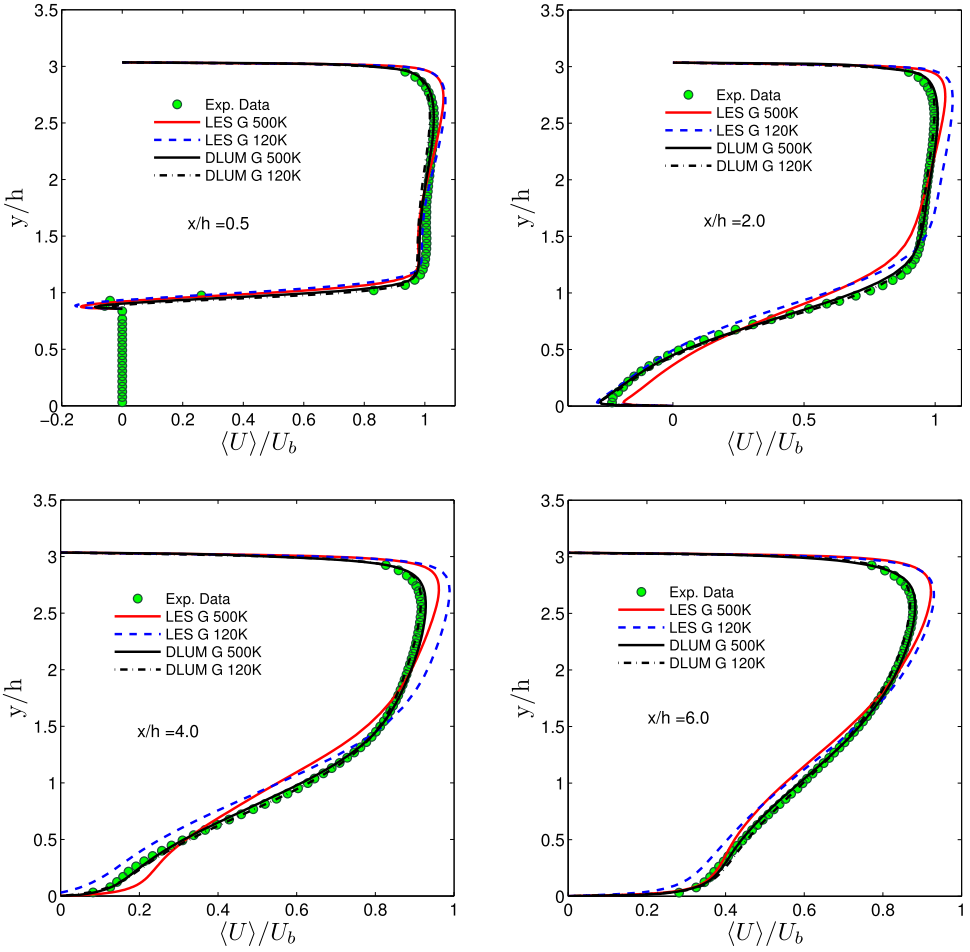

FIG. 23. The advantage of the DLUM compared to LES on very coarse grids. Streamwise velocity profiles are shown at different axial positions.

the 500K and 120K results. We also observed that using the 120K grid, the DLUM is capable to correctly capture the recirculation bubble. It predicts the reattachment point at $x/h = 3.9$ with a 4% discrepancy to the experimental data. Therefore, also with regard to the question of how a relatively coarse grid affects simulation results, we see significant advantages of the DLUM compared to pure LES.

VII. DLUM VERSUS LES: COST

We complete the comparison of our new DLUM with LES by analyzing the computational cost required for the use of both methods. The LES-to-DLUM computational cost ratio is denoted by G, which is the gain factor of performing hybrid RANS-LES simulations. It is calculated by

$$G = \frac{N_{LES}}{N_{DLUM}} \frac{n_{LES}}{n_{DLUM}} \frac{t^*_{LES}}{t^*_{DLUM}} = \frac{N_{LES}}{N_{DLUM}} \frac{\Delta t_{DLUM}}{\Delta t_{LES}} \frac{t^*_{LES}}{t^*_{DLUM}}. \tag{22}$$

Here, N is the number of cells applied in the simulation, n is the number of iterations performed, and t^* is the computer time per iteration. The number n of iterations is related to the time step Δt applied in computations and the total physical simulation time T via $T = n\Delta t$. Combined with $T_{LES} = T_{DLUM}$, the latter relation implies the right-hand side of Eq. (22).

The number N of cells applied depends on the Reynolds number: by increasing the Reynolds number we have to use more computational cells to meet, for example, the y^+ grid resolution criterion. The time step Δt applied is also a function of the Reynolds number: we have to meet the maximum CFL number criterion to ensure the stability of numerical simulation. However, the ratio t^*_{LES}/t^*_{DLUM} in Eq. (22) is independent of the Reynolds number, it only depends on the number of equations involved and the computational time needed for the numerical integration of equations. The DLUM and pure LES differ by the fact that the use of the DLUM involves the ω equation, and an elliptic equation has to be solved to obtain the damping function C_μ. We found that the LES to DLUM ratio of computer cost per iteration is given by

$$\frac{t^*_{LES}}{t^*_{DLUM}} \approx 0.96. \tag{23}$$

This ratio was found by calculating the execution time of 10 000 iterations for LES and DLUM simulations for the same Reynolds number using the same grid and the same time step in parallel computations with 16 equal processors.

To calculate the other cost factors ($N_{LES}, N_{DLUM}, \Delta t_{LES}, \Delta t_{DLUM}$) in Eq. (22), simulations have been performed using DLUM and pure LES for three different Reynolds numbers (10 600, 19 000, and 37 000). For each Reynolds number, the criterion for choosing the LES grid was a grid that has a maximum y^+ less than one. Regarding the DLUM grid, we used the criterion that the averaged y^+ at the bottom has to be about 2. On this basis, the corresponding LES grids have 5, 10, and 20×10^6 cells, and the DLUM grids have 0.25, 0.35, and 0.5×10^6 cells for Reynolds numbers 10 600, 19 000, and 37 000, respectively. The criterion for choosing the time step was that the maximum CFL number should not exceed 0.5. Based on this criterion, we applied time steps that are given in Table IV together with the other parameters of this cost analysis.

TABLE IV. Cost analysis parameter of DLUM and LES simulations for three Reynolds numbers.

	$N/10^6$		$\Delta t/10^{-3}$	
Re	LES	DLUM	LES	DLUM
10 600	5	0.25	3	10
19 000	10	0.35	1.8	8
37 000	20	0.5	1	6

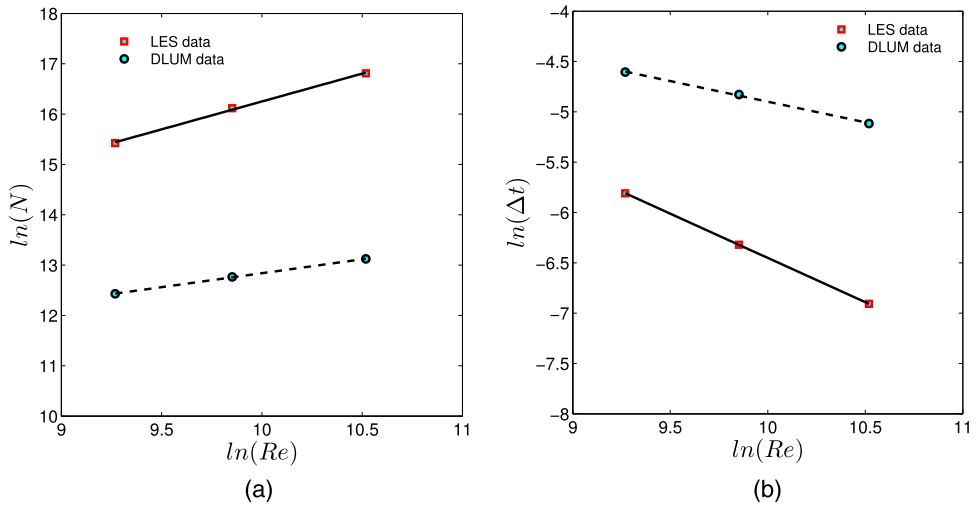

FIG. 24. DLUM versus LES cost comparison: The dependence of the number of grid cells and time steps on the Reynolds number. Squares and circles show LES and DLUM data, respectively. Solid and dashed lines show the linear least squares fits to computational results.

Figure 24 shows the dependence of the number N of grid cells and time steps Δt for LES and DLUM simulations depending on the Reynolds number. It can be observed that $ln(N)$ and $ln(\Delta t)$ are basically linear functions of $ln(Re)$. Therefore, the number of grid cells N and time steps Δt can be written as power law functions of Re,

$$N = aRe^{b}, \tag{24}$$

$$\Delta t = cRe^{d}. \tag{25}$$

The model parameters a, b, c, d can be obtained by a linear regression of data points in Fig. 24. Accordingly, the power functions for N and Δt for LES and DLUM simulations are given by

$$N_{LES} = 177Re^{1.11}, \quad N_{DLUM} = 1478Re^{0.554}, \tag{26}$$

$$\Delta t_{LES} = 10.36Re^{-0.879}, \quad \Delta t_{DLUM} = 0.45Re^{-0.409}. \tag{27}$$

Therefore, the corresponding DLUM versus LES gain factors are given by

$$\frac{N_{LES}}{N_{DLUM}} = 0.12Re^{0.556}, \tag{28}$$

$$\frac{\Delta t_{DLUM}}{\Delta t_{LES}} = 0.043Re^{0.47}. \tag{29}$$

According to Eq. (22), the gain factor of performing hybrid RANS-LES simulations instead of LES is then given by

$$G = \frac{N_{LES}}{N_{DLUM}} \frac{\Delta t_{DLUM}}{\Delta t_{LES}} \frac{t^*_{LES}}{t^*_{DLUM}} = 0.00\,495Re^{1.026} \approx Re/200. \tag{30}$$

At a relatively low Reynolds number, there is no significant cost gain advantage related to the use of the DLUM, but at a relatively high Reynolds number, the computational gain of using the DLUM can be huge, as illustrated by the following example. A fine grid LES simulation of a separated flow at a Reynolds number of 10^6 requires about 800×10^6 cells, whereas a corresponding DLUM simulation requires about 3×10^6 cells. The gain factor of the DLUM arising from the grid is about 260, and the related gain factor originated from the time step is about 28. By involving the cost factor related to the computer time per iteration, the total gain factor of using the DLUM is about 7000. This example shows that the cost reduction related to the use of the DLUM enables simulations of complex flows at realistic, high Reynolds numbers.

VIII. SUMMARY

The development of hybrid RANS-LES methods is seen to be a very promising approach to enable efficient simulations of high Reynolds number turbulent flows involving flow separation. We presented a new hybrid RANS-LES method: the combination of a hybrid RANS-LES method with dynamic LES. The deterministic model obtained in this way is theoretically well based: it is systematically derived as a consequence of an underlying realizable stochastic turbulence model.[46,43,44,47] It is applied to a high Reynolds number flow involving both attached and separated flow regimes. Its performance is compared to pure LES, pure RANS, several other hybrid RANS-LES, and experimental observations.

To clarify the standard of pure dynamic LES used for the evaluation of our hybrid RANS-LES, we analyzed in Sec. IV the resolution ability of our LES on several grids. By addressing this question first on the basis of usual criteria applied to attached flows we concluded that our fine grid LES is not fully resolved. A fully resolved LES would have required a grid with 120M grid points, which is far above our available computational resources. We addressed the same question on the basis of correlation function analysis. Our conclusion was similar to the conclusion obtained using usual flow resolution criteria: our fine grid still does not enable fully resolved LES. Given the huge computational cost of LES for high Reynolds number turbulent flows, this setup may be considered to be the usual case, meaning that experimental data are required for the evaluation of computational methods.

We continued in Sec. V with an analysis of the suitability and main features of the computational setup of our hybrid RANS-LES method. In particular, three hybrid RANS-LES methods were presented: our standard hybrid model (DLUM), and two modified versions (DLUM-NW, DLUM-FW). The better suitability of the DLUM compared to the other two DLUM versions was shown in Sec. V A based on a discussion of characteristic length scales. Based on studying the DLUM performance on several grids and for different filter width definitions, we determined the 500K grid to be our standard DLUM grid and the maximum filter width to be the best filter width for our hybrid RANS-LES simulations. We illustrated a characteristic feature of the RANS-LES transition implied by our hybrid model, in particular its fluctuations in space and time in varying regions close to the wall.

Our main results regarding the accuracy of our hybrid RANS-LES model were presented in Sec. VI by using experimental data for comparisons. First, by considering streamlines we concluded that our DLUM reflects the typical flow structures more accurately than the fine grid LES. Second, by considering mean velocity and Reynolds stress distributions, we showed that our DLUM provides almost perfect predictions of the most important flow characteristics, mean velocities. Its performance regarding the prediction of Reynolds stresses is very good. On the other hand, the performance of under-resolved LES is by far not as good as the DLUM performance: significant discrepancies to experimental data can be seen already by looking at the mean velocity profiles. Third, we analyzed the reasons for LES performance deficiencies. We concluded that the significant difference of the DLUM concept compared to LES is the ability to respond to a changing resolution with adequate turbulent viscosity changes. However, this difference does not ensure a perfect performance of DLUM versions; their performance in simulations still can be comparable to RANS or LES. The essential requirement is to ensure a physically correct turbulence length scale specification, in particular, under the presence of interacting RANS and LES modes (which represents a nontrivial problem). Based on conceptual arguments and our simulation results, we also concluded that our DLUM does not suffer from the gray area problem, which is usually considered to represent the biggest challenge of hybrid RANS-LES methods. Fourth, we compared LES and the DLUM performance on a coarse grid, which is often simply required to deal with simulations of very high Reynolds number flows. Also in this regard, the DLUM offers significant advantages compared to LES: DLUM velocity fields are hardly affected by the grid, whereas LES velocity fields reveal significant shortcomings. It is interesting to note that the DLUM still accurately captures the recirculation region structure.

Our main results regarding the cost advantage of our hybrid RANS-LES method were presented in Sec. VII. We concluded that the cost gain of DLUM compared to LES scales with $Re/200$.

For a realistic Reynolds number of 10^6, for example, the DLUM cost gain is about 7000. This huge cost gain for realistic Reynolds numbers enables accurate and feasible simulations that cannot be performed otherwise.

The overall conclusions of this analysis can be summarized as follows. The use of the hybrid RANS-LES model presented here offers huge cost reductions of very high Reynolds number flow simulations compared to LES, it is much more accurate than RANS, and more accurate than under-resolved LES. From a more general view point, the DLUM is more reliable than LES for high Reynolds number flows, which often faces the nontrivial question[83,84] of how well resolving the LES actually is. We identified the reason for the superior performance of the DLUM compared to LES: it is the DLUM's ability to respond to a changing resolution with adequate turbulent viscosity changes by ensuring simultaneously a physically correct turbulence length scale specification under the presence of interacting RANS and LES modes. Obviously, it would be highly beneficial to obtain more evidence for the advantages of the DLUM with respect to highly complex and very high Reynolds number flow simulations.

ACKNOWLEDGMENTS

The authors would like to acknowledge support through NASA's NRA research opportunities in aeronautics program (Grant No. NNX12AJ71A) with Dr. P. Balakumar as the technical officer. Fruitful discussions with Dr. P. Balakumar significantly contributed to the success of this project. We are very thankful for computational resources provided by the Advanced Research Computing Center[92] and the Wyoming-NCAR Alliance[93] at the University of Wyoming. We would like to thank the referees for their helpful suggestions for improvements.

[1] P. R. Spalart, W. H. Jou, M. Strelets, and S. R. Allmaras, "Comments on the feasibility of LES for wings, and on a hybrid RANS/LES approach," in *1st AFOSR International Conference on DNS/LES* (Greyden Press, Columbus, Ruston, LA, USA, 1997), pp. 4–8.
[2] J. Bodart and J. Larsson, "Wall-modeled large eddy simulation in complex geometries with application to high-lift devices," in *Center for Turbulence Research Proceedings of the Summer Program 2011* (2011), pp. 37–48.
[3] S. Kawai and J. Larsson, "Dynamic non-equilibrium wall-modeling for large eddy simulation at high Reynolds numbers," Phys. Fluids **25**(1), 015105 (2013).
[4] G. I. Park and P. Moin, "An improved dynamic non-equilibrium wall-model for large eddy simulation," Phys. Fluids **26**(1), 015108 (2014).
[5] S. T. Bose and P. Moin, "A dynamic slip boundary condition for wall-modeled large-eddy simulation," Phys. Fluids **26**(1), 015104 (2014).
[6] P. Balakumar, G. I. Park, and B. Pierce, "DNS, LES and wall-modeled LES of separating flow over periodic hills," in *Center for Turbulence Research Proceedings of the Summer Program 2014* (2014), pp. 407–415.
[7] W. Cheng, D. I. Pullin, and R. Samtaney, "Large-eddy simulation of separation and reattachment of a flat plate turbulent boundary layer," J. Fluid Mech. **785**, 78–108 (2015).
[8] X. I. A. Yang, J. Sadique, R. Mittal, and C. Meneveau, "Integral wall model for large eddy simulations of wall-bounded turbulent flows," Phys. Fluids **27**(2), 025112 (2015).
[9] A. Travin, M. Shur, M. Strelets, and P. Spalart, "Detached-eddy simulations past a circular cylinder," Flow, Turbul. Combust. **63**(1), 293–313 (2000).
[10] L. S. Hedges, A. K. Travin, and P. R. Spalart, "Detached-eddy simulations over a simplified landing gear," J. Fluids Eng. **124**(2), 413–423 (2002).
[11] P. R. Spalart, S. Deck, M. L. Shur, K. D. Squires, M. K. Strelets, and A. Travin, "A new version of detached-eddy simulation, resistant to ambiguous grid densities," Theor. Comput. Fluid Dyn. **20**(3), 181–195 (2006).
[12] M. Shur, P. Spalart, M. Strelets, and A. Travin, "A hybrid RANS-LES model with delayed DES and wall-modeled LES capabilities," Int. J. Heat Fluid Flow **29**, 1638–1649 (2008).
[13] P. Spalart, "Detached-eddy simulation," Annu. Rev. Fluid Mech. **41**(2), 181–202 (2009).
[14] L. Davidson and S. H. Peng, "Hybrid LES-RANS modelling: A one-equation SGS model combined with a k-ω model for predicting recirculating flows," Int. J. Numer. Methods Fluids **43**(9), 1003–1018 (2003).
[15] F. Hamba, "A hybrid RANS/LES simulation of turbulent channel flow," Theor. Comput. Fluid Dyn. **16**(5), 387–403 (2003).
[16] F. Hamba, "Log-layer mismatch and commutation error in hybrid RANS/LES simulation of channel flow," Int. J. Heat Fluid Flow **30**(1), 20–31 (2009).
[17] P. G. Tucker and L. Davidson, "Zonal *k–l* based large eddy simulations," Comput. Fluids **33**(2), 267–287 (2004).
[18] R. Schiestel and A. Dejoan, "Towards a new partially integrated transport model for coarse grid and unsteady turbulent flow simulations," Theor. Comput. Fluid Dyn. **18**, 443–468 (2005).
[19] F. R. Menter and Y. Egorov, "SAS turbulence modelling of technical flows," in *Proceedings of 6th International ERCOFTAC Workshop on Direct and Large-Eddy Simulation, Poitiers, France, 2005*, Vol. 10, pp. 687–694.
[20] F. R. Menter and Y. Egorov, "The scale-adaptive simulation method for unsteady turbulent flow predictions. I: Theory and model description," Flow, Turbul. Combust. **85**, 113–138 (2010).

[21] C. De Langhe, B. Merci, and E. Dick, "Hybrid RANS/LES modelling with an approximate renormalization group. I: Model development," J. Turbul. **6**(13), 1–19 (2005).
[22] C. De Langhe, B. Merci, K. Lodefier, and E. Dick, "Hybrid RANS/LES modelling with an approximate renormalization group. II: Applications," J. Turbul. **6**(14), 1–17 (2005).
[23] C. De Langhe, B. Merci, and E. Dick, "Application of a RG hybrid RANS/LES model to swirling confined turbulent jets," J. Turbul. **7**(56), 1–19 (2006).
[24] C. De Langhe, J. Bigda, K. Lodefier, and E. Dick, "One-equation RG hybrid RANS/LES computation of a turbulent impinging jet," J. Turbul. **9**(16), 1–19 (2008).
[25] M. Breuer, B. Jaffrézic, and K. Arora, "Hybrid LES-RANS technique based on a one-equation near-wall model," Theor. Comput. Fluid Dyn. **22**(3), 157–187 (2008).
[26] J. Fröhlich and D. V. Terzi, "Hybrid LES/RANS methods for the simulation of turbulent flows," Prog. Aerosp. Sci. **44**(5), 349–377 (2008).
[27] C. G. Speziale, "Turbulence modeling for time-dependent RANS and VLES: A review," AIAA J. **36**(2), 173–184 (1998).
[28] H. F. Fasel, D. A. V. Terzi, and R. D. Sandberg, "A methodology for simulating compressible turbulent flows," J. Appl. Mech. **73**(3), 405–412 (2006).
[29] M. Germano, "Properties of the hybrid RANS/LES filter," Theor. Comput. Fluid Dyn. **17**(4), 225–231 (2004).
[30] P. Sagaut and M. Germano, "On the filtering paradigm for LES of flows with discontinuities," J. Turbul. **6**(23), 1–9 (2005).
[31] M. Sánchez-Rocha and S. Menon, "The compressible hybrid RANS/LES formulation using an additive operator," J. Comput. Phys. **228**(6), 2037–2062 (2009).
[32] B. Rajamani and J. Kim, "A hybrid-filter approach to turbulence simulation," Flow, Turbul. Combust. **85**(3-4), 1–21 (2010).
[33] A. Fadai-Ghotbi, C. Friess, R. Manceau, and J. Borée, "A seamless hybrid RANS-LES model based on transport equations for the subgrid stresses and elliptic blending," Phys. Fluids **22**, 055104 (2010).
[34] M. Sánchez-Rocha and S. Menon, "An order-of-magnitude approximation for the hybrid terms in the compressible hybrid RANS/LES governing equations," J. Turbul. **12**(16), 1–22 (2011).
[35] Z. Yin, K. Reddy, and P. Durbin, "On the dynamic computation of the model constant in delayed detached eddy simulation," Phys. Fluids **27**(2), 025105 (2015).
[36] S. S. Girimaji, "Partially-averaged Navier-Stokes model for turbulence: A Reynolds-averaged Navier-Stokes to direct numerical simulation bridging method," J. Appl. Mech. **73**, 413–421 (2006).
[37] S. Lakshmipathy and S. Girimaji, "Extension of Boussinesq turbulence constitutive relation for bridging methods," J. Turbul. **8**(31), 1–21 (2007).
[38] A. Frendi, A. Tosh, and S. Girimaji, "Flow past a backward-facing step: Comparison of PANS, DES and URANS results with experiments," Int. J. Comput. Methods Eng. Sci. Mech. **8**(1), 23–38 (2007).
[39] S. Lakshmipathy and S. Girimaji, "Partially averaged Navier–Stokes (PANS) method for turbulence simulations: Flow past a circular cylinder," J. Fluids Eng. **132**, 121202 (2010).
[40] E. Jeong and S. Girimaji, "Partially averaged Navier–Stokes (PANS) method for turbulence simulations: Flow past a square cylinder," J. Fluids Eng. **132**, 121203 (2010).
[41] B. Huang and G. Wang, "Partially averaged Navier-Stokes method for time-dependent turbulent cavitating flows," J. Hydrodyn. Ser. B **23**(1), 26–33 (2011).
[42] A. Fadai-Ghotbi, C. Friess, R. Manceau, T. Gatski, and J. Boree, "Temporal filtering: A consistent formalism for seamless hybrid RANS-LES modeling in inhomogeneous turbulence," Int. J. Heat Fluid Flow **31**, 378–389 (2010).
[43] S. Heinz, *Statistical Mechanics of Turbulent Flows*, 1st ed. (Springer-Verlag, Berlin, Heidelberg, New York, Tokyo, 2003).
[44] S. Heinz, "Unified turbulence models for LES and RANS, FDF and PDF simulations," Theor. Comput. Fluid Dyn. **21**(2), 99–118 (2007).
[45] H. Gopalan, S. Heinz, and M. Stöllinger, "A unified RANS-LES model: Computational development, accuracy and cost," J. Comput. Phys. **249**, 249–274 (2013).
[46] S. Heinz, "On Fokker–Planck equations for turbulent reacting flows. II. Filter density function for large eddy simulation," Flow, Turbul. Combust. **70**(1), 153–181 (2003).
[47] S. Heinz, "Realizability of dynamic subgrid-scale stress models via stochastic analysis," Monte Carlo Methods Appl. **14**(4), 311–329 (2008).
[48] S. Heinz and H. Gopalan, "Realizable versus non-realizable dynamic subgrid-scale stress models," Phys. Fluids **24**(11), 115105 (2012).
[49] S. Heinz, M. Stoellinger, and H. Gopalan, "Unified RANS-LES simulations of turbulent swirling jets and channel flows," in *Progress in Hybrid RANS-LES Modelling*, Notes on Numerical Fluid Mechanics and Multidisciplinary Design Vol. 130 (Springer, Cham, Heidelberg, New York, Dordrecht, London, 2015), pp. 265–275.
[50] E. Kazemi and S. Heinz, "Dynamic large eddy simulations of the Ekman layer based on stochastic analysis," Int. J. Nonlinear Sci. Numer. Simul. **17**(2), 77–98 (2016).
[51] J. L. Lumley, "Computational modeling of turbulent flows," Adv. Appl. Mech. **18**, 123–175 (1978).
[52] U. Schumann, "Realizability of Reynolds stress turbulence models," Phys. Fluids **20**(5), 721–725 (1977).
[53] R. D. Vachat, "Realizability inequalities in turbulent flows," Phys. Fluids **20**(4), 551–556 (1977).
[54] C. Fureby and G. Tabor, "Mathematical and physical constraints on large-eddy simulations," Theor. Comput. Fluid Dyn. **9**(2), 85–102 (1997).
[55] S. Ghosal, "Mathematical and physical constraints on large-eddy simulation of turbulence," AIAA J. **37**(4), 425–433 (1999).
[56] B. Vreman, B. Geurts, and H. Kuerten, "Realizability conditions for the turbulent stress tensor in large-eddy simulation," J. Fluid Mech. **278**, 351–362 (1994).
[57] P. A. Durbin and C. G. Speziale, "Realizability of second-moment closure via stochastic analysis," J. Fluid Mech. **280**, 395–407 (1994).
[58] S. S. Girimaji, "A new perspective on realizability of turbulence models," J. Fluid Mech. **512**, 191–210 (2004).
[59] S. B. Pope, "PDF methods for turbulent reactive flows," Prog. Energy Combust. Sci. **11**(2), 119–192 (1985).

[60] S. B. Pope, "On the relationship between stochastic Lagrangian models of turbulence and second-moment closures," Phys. Fluids **6**(2), 973–985 (1994).
[61] C. G. Speziale, R. Abid, and P. A. Durbin, "New results on the realizability of Reynolds stress turbulence closures," ICASE Report No. 93-76, 1993, 1–47.
[62] H. A. Wouters, T. W. J. Peeters, and D. Roekaerts, "On the existence of a generalized L angevin model representation for second-moment closures," Phys. Fluids **8**(7), 1702–1704 (1996).
[63] J. Bredberg, S. H. Peng, and L. Davidson, "An improved k- ω turbulence model applied to recirculating flows," Int. J. Heat Fluid Flow **23**(6), 731–743 (2002).
[64] See http://www.openfoam.com for Openfoam, the open source CFD toolbox; accessed August 5, 2015.
[65] R. I. Issa, "Solution of the implicitly discretised fluid flow equations by operator-splitting," J. Comput. Phys. **62**(1), 40–65 (1986).
[66] C. P. Mellen, J. Frohlich, and W. Rodi, "Large-eddy simulation of the flow over periodic hills," in *Proceedings of 16th IMACS World Congress*, *Lausanne, Switzerland*, *2000*, pp. 1–6.
[67] G. Almeida, D. Durao, and M. Heitor, "Wake flows behind two dimensional model hills," Exp. Therm. Fluid Sci. **7**, 87–101 (1993).
[68] L. Temmerman and M. A. Leschziner, "Large eddy simulation of separated flow in a streamwise periodic channel constriction," in *Proceedings of 2nd International Symposium of Turbulence and Shear Flow Phenomena* (KTH, Stockholm, 2001), pp. 399–404.
[69] L. Temmerman, M. A. Leschziner, C. P. Mellen, and J. Frohlich, "Investigation of wall-function approximations and subgrid-scale models in large eddy simulation of separated flow in a channel with streamwise periodic constrictions," Int. J. Heat Fluid Flow **24**, 157–180 (2005).
[70] S. Jakirlic, R. J. Zürker, and C. Tropea, "Report on 9th ERCOFTAC/IAHR /COST workshop on refined turbulence modelling," in *ERCOFTAC Bulletin* (Darmstadt University of Technology, 2001), pp. 36–43.
[71] Y. J. Jang, M. A. Leschziner, K. Abe, and L. Temmerman, "Investigation of anisotropy-resolving turbulence models by reference to highly-resolved LES data for separated flow," Flow, Turbul. Combust. **69**, 161–203 (2002).
[72] J. Fröhlich, C. P. Mellen, W. Rodi, L. Temmerman, and M. A. Leschziner, "Highly resolved large-eddy simulation of separated flow in a channel with streamwise periodic constrictions," J. Fluid Mech. **526**, 19–66 (2005).
[73] C. Rapp and M. Manhart, "Experimental investigations on the turbulent flow over a periodic hill geometry," in *5th International Symposium Turbulence and Shear Flow Phenomena*, *Garching, Germany*, *2001*, Vol. 2, pp. 649–654.
[74] C. Rapp, F. Pfleger, and M. Manhart, "New experimental results for a LES benchmark case," in *Direct and Large-Eddy Simulation VII*, Volume 13 of ERCOFTAC Series, edited by V. Armenio, B. Geurts, and J. Fröhlich (Springer, Netherlands, 2010), pp. 69–74.
[75] M. Breuer, N. Peller, C. Rapp, and M. Manhart, "Flow over periodic hills—Numerical and experimental study in a wide range of Reynolds numbers," Comput. Fluids **38**, 433–457 (2009).
[76] S. Jakirlic, S. Saric, G. Kadavelil, E. Sirbubalo, B. Basara, and B. Chaouat, "SGS modelling in LES of wall-bounded flows using transport RANS models: From a zonal to a seamless hybrid LES/RANS method," in *Proceeding of the 6th Symposium on Turbulent Shear Flow Phenomena*, *Seoul, Korea*, *2009*, Vol. 3, pp. 1057–1062.
[77] B. Chaouat and R. Schiestel, "A new partially integrated transport model for subgrid-scale stresses and dissipation rate for turbulent developing flows," Phys. Fluids **17**, 065106 (2005).
[78] B. Chaouat, "Subfilter-scale transport model for hybrid RANS/LES simulations applied to a complex bounded flow," J. Turbul. **11**(51), 1–30 (2010).
[79] C. Rapp and M. Manhart, "Flow over periodic hills: An experimental study," Exp. Fluids **51**, 247–269 (2011).
[80] See http://qnet-ercoftac.cfms.org.uk/w/index.php/UFR_3-30_Test_Case for Ercoftac; accessed August 5, 2015.
[81] B. Chaouat and R. Schiestel, "Hybrid RANS/LES simulations of the turbulent flow over periodic hills at high Reynolds number using the PITM method," Comput. Fluids **84**, 279–300 (2013).
[82] U. Piomelli and J. R. Chasnov, "Large-eddy simulations: Theory and applications," in *Turbulence and Transition Modeling*, edited by M. Hallback, D. Henningson, A. Johansson, and P. Alfredson (Kluwer, 1996), pp. 269–331.
[83] L. Davidson, "Large eddy simulations: How to evaluate resolution," Int. J. Heat Fluid Flow **30**(5), 1016–1025 (2009).
[84] L. Davidson, "How to estimate the resolution of an LES of recirculating flow," in *Quality and Reliability of Large-Eddy Simulations II*, edited by M. V. Salvetti, B. Geurts, J. Meyers, and P. Sagaut, Ercoftac Series (Springer, 2010), Vol. 16, pp. 269–286.
[85] P. Durbin, "Limiters and wall treatments in applied turbulence modeling," Fluid Dyn. Res. **40**, 012203 (2009).
[86] P. A. Durbin, "A Reynolds-stress model for near-wall turbulence," J. Fluid Mech. **249**, 465–498 (1993).
[87] R. Manceau and K. Hanjalic, "Elliptic blending model: A new near-wall Reynolds-stress turbulence closure," Phys. Fluids **14**(2), 744–754 (2002).
[88] R. Manceau, "Recent progress in the development of the elliptic blending Reynolds-stress model," Int. J. Heat Fluid Flow **51**, 195–220 (2015).
[89] M. Stoellinger, R. Roy, and S. Heinz, "Unified RANS-LES method based on second-order closure," in *International Symposium on Turbulence and Shear Flow Phenomena (TSFP-9)*, *Melbourne, Australia*, *2015*, pp. P44/1–P44/6.
[90] M. Waclawczyk, J. Pozorski, and J. P. Minier, "Probability density function computation of turbulent flows with a new near-wall model," Phys. Fluids **16**, 1410–1422 (2004).
[91] P. Spalart, "Strategies for turbulence modelling and simulations," Int. J. Heat Fluid Flow **21**, 252–263 (2000).
[92] See http://n2t.net/ark:/85786/m4159c for Advanced Research Computing Center. 2012. Mount Moran: IBM System X cluster. Laramie, WY: University of Wyoming; accessed May 5, 2016.
[93] See http://n2t.net/ark:/85065/d7wd3xhc for Computational and Information Systems Laboratory. 2012. Yellowstone: IBM iDataPlex System (Wyoming-NCAR Alliance). Boulder, CO: National Center for Atmospheric Research; accessed May 05, 2016.